Research Square

Preprints are preliminary reports that have not undergone peer review.
They should not be considered conclusive, used to inform clinical practice,
or referenced by the media as validated information.

A Large-Scale Anatomically and Electrophysiologically Constrained Model of Hippocampus at Behavioral Time Scales

Dong Song

dsong@usc.edu

University of Southern California https://orcid.org/0000-0002-6179-1120

Gene Yu

Duke University

Chenlin Xu

University of Southern California

Lars Niedermeier

Niedermeier Consulting

Xiang Zhang

University of Southern California

Hongwei Dong

University of California, Los Angeles

Article

Keywords:

Posted Date: October 22nd, 2026

DOI: https://doi.org/10.21203/rs.3.rs-11447128/v1

License: This work is licensed under a Creative Commons Attribution 4.0 International License.
Read Full License

Additional Declarations: There is **NO** Competing Interest.

A Large-Scale Anatomically and Electrophysiologically Constrained Model of Hippocampus at Behavioral Time Scales

Gene J. Yu[1,6], Chenlin Xu[2,6], Lars Niedermeier[3], Xiang Zhang[2], Hongwei Dong[4], and Dong Song[2,5]

[1]Department of Biomedical Engineering, Duke University, Durham, NC 27708, USA; [2]Alfred E. Mann Department of Biomedical Engineering, University of Southern California, Los Angeles, CA 90089, USA; [3]Niedermeier Consulting, Stäfa, Zürich, Switzerland; [4]Department of Neurology, University of California, Los Angeles, Los Angeles, CA 90095, USA; [5]Department of Neurological Surgery, University of Southern California, Los Angeles, CA 90089, USA; [6]These authors contributed equally: Gene J. Yu, Chenlin Xu.

*Correspondence and proof should be sent to:

Dong Song
403 Hedco Neuroscience Building
University of Southern California
Los Angeles, CA 90089
Tel: 213-740-8063
E-mail: dsong@usc.edu

Abstract

Large-scale mechanistic brain models remain challenging to construct from heterogeneous anatomical and physiological data, simulate over behavioral timescales, and optimize against network-level activity. Here, we introduce a GPU-accelerated computational framework that transforms population-level anatomical measurements into explicit, single-neuron-resolution connectivity and integrates cell-type-specific neuronal and synaptic dynamics. A two-stage optimization strategy combines calibration against unitary synaptic responses with physiologically informed network-level optimization, using online parameter updates during continuous simulation. We demonstrate the framework in a hippocampal network comprising approximately 250,000 neurons, 20 million synapses, and 25 neuronal types. The optimized network reproduces population firing statistics and oscillatory dynamics and generates spatially selective hippocampal activity without explicit place-field tuning. The model achieves a runtime factor of approximately 20 relative to biological time, with scaling analysis predicting approximately 50 at full scale, supporting simulations over behavioral timescales. This framework provides a scalable approach for constructing and functionally optimizing anatomically constrained neural circuit models.

Introduction

Understanding hippocampal function requires computational models that preserve anatomical and electrophysiological realism and can simulate behaviorally relevant timescales. The hippocampus integrates spatial[1–5], temporal[6–8], and sensory[9–13] information through complex neuronal networks across its subfields, giving rise to memory encoding[14–18], consolidation[19–21], and navigation[22–24] behaviors that unfold over seconds to minutes. While mechanistic spiking network models have yielded important insights into local circuit dynamics and synaptic mechanisms, existing modeling frameworks face a fundamental limitation: achieving anatomical fidelity, large-scale network size, and long simulation durations simultaneously remains challenging. Models that preserve detailed anatomy are typically restricted to sub-second simulations[25–32], whereas models capable of extended simulations often rely on simplified or abstract connectivity[33–36]. This tradeoff has limited the ability of realistic hippocampal models to address behaviorally relevant questions.

Here we present a GPU-accelerated modeling framework for anatomically and electrophysiologically constrained simulations of the hippocampus (**Fig. 1**). The framework integrates multiscale anatomical data with biophysically grounded spiking dynamics, enabling biologically realistic simulations of large hippocampal networks over behaviorally relevant timescales without sacrificing anatomical fidelity.

The framework is built upon a connectivity-generation pipeline that constructs single-neuron-resolution networks directly from experimental anatomical data[31,37–40]. Previous studies have revealed the highly differentiated molecular and anatomical organization of hippocampal circuits, including distinct functional domains along the longitudinal axis and topographically organized projection networks[41–43]. Comprehensive knowledge bases such as Hippocampome.org have further characterized hippocampal neuron types based on their morphological, molecular, and electrophysiological properties[44,45]. Building on these advances, our framework integrates cell-type-specific anatomical properties, tracer-derived projection maps, axonal density distributions, and lamina-specific convergence and divergence constraints to generate anatomically organized intra- and inter-regional connectivity. Rather than relying on manually specified connection patterns

or generic statistical connectivity rules, the resulting network preserves experimentally derived structural constraints while explicitly representing synaptic connections between individual neurons.

To support long-duration simulations of these networks, the framework leverages GPU acceleration to efficiently simulate hundreds of thousands to millions of neurons and tens of millions to billions of synapses. This computational scalability enables investigations into sustained hippocampal dynamics, including oscillations, navigation-related dynamics, and other temporally extended computations that are difficult to study with existing large-scale spiking models.

The framework further incorporates a hierarchical optimization strategy that constrains model behavior at both the single-neuron and neuronal-network levels. Synaptic parameters are first optimized to reproduce experimentally measured unitary postsynaptic potentials and intrinsic firing properties and are subsequently refined to match population-level electrophysiological targets such as firing rates, spatial correlation, and oscillatory activity. Crucially, network optimization is performed online, allowing synaptic weights to be updated during simulation without rebuilding or restarting the model.

Network-level optimization is performed using a novel physiologically informed Nelder–Mead simplex method. The Nelder–Mead component provides robustness in regimes where gradients are unavailable or unreliable, whereas physiological insights accelerate convergence by providing targeted parameter initialization and simplex vertices during optimization. This hybrid strategy scales favorably with the complexity of the optimization objective, making it well-suited for fitting nonlinear, complex, emergent network dynamics and functional mappings in large-scale spiking models. Together, these features enable stable and efficient fitting of complex hippocampal network behavior without compromising simulation performance or biological realism.

We demonstrate the framework using a one-tenth-scale model of the rat hippocampus containing approximately 250,000 neurons and 20 million synapses. The model reproduces key anatomical and electrophysiological features of hippocampal circuits while supporting simulations ranging from tens of seconds to hours. Because the

framework scales directly to full hippocampal size without architectural modification, it provides a practical path toward whole-hippocampus simulations at behaviorally relevant timescales.

Together, this framework establishes a general platform for anatomically and electrophysiologically constrained large-scale brain simulations. By bridging single-neuron physiology, circuit architecture, emergent network dynamics, and systems-level function, it enables mechanistic studies of hippocampal computation across spatial and temporal scales and can be readily extended to other anatomically organized brain regions.

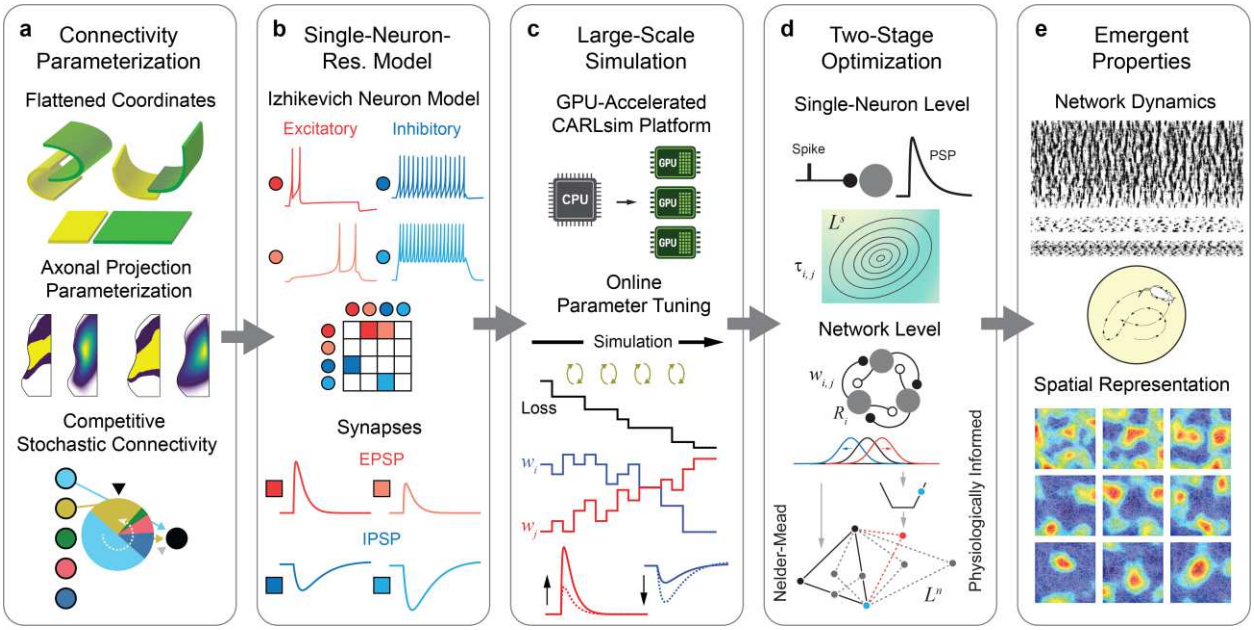


Fig. 1 | Overview of the anatomically constrained, large-scale hippocampal network modeling framework. a, Connectivity parameterization. Hippocampal anatomy is transformed into flattened spatial coordinates, and experimentally derived axonal projection patterns are parameterized as continuous probability density functions. Single-neuron-resolution connectivity is generated through anatomically constrained, competitive stochastic sampling. **b,** Single-neuron-resolution modeling. Neuronal dynamics are represented using the nine-parameter Izhikevich model, with cell-type-specific electrophysiological properties and conductance-based excitatory and inhibitory synapses. **c,** Large-scale simulation. The GPU-accelerated CARLsim6 platform enables efficient simulation of large spiking networks and online synaptic parameter updating without interrupting ongoing network activity. **d,** Two-stage optimization. Synaptic parameters are first calibrated against experimentally measured postsynaptic potentials at the single-neuron level and subsequently optimized at the network level to reproduce physiologically constrained population firing rates, correlations, and oscillatory dynamics. **e,** Emergent network properties. The resulting model generates biologically relevant network dynamics and spatially selective firing patterns during simulated behavior, demonstrating the emergence of higher-level functional properties from anatomically and electrophysiologically constrained neuronal circuits.

Results

Anatomically constrained single-neuron–level connectivity of the whole hippocampus

To reconstruct hippocampal connectivity at single-neuron resolution, we developed an anatomically constrained modeling framework that transforms population-level anatomical tracer data into explicit synaptic connections between individual neurons (**Fig. 1a**). Although tracer studies provide spatial maps of axonal projections and terminal fields, they do not resolve connectivity between individual neurons. Our framework bridges this gap by integrating tracer-derived projection maps, probabilistic axonal terminal distributions, and anatomical constraints on convergence, divergence, and laminar targeting to generate biologically realistic single-neuron connectivity (**Fig. 2a, b, c**). This pipeline preserves experimentally observed projection topography while producing explicit synaptic networks suitable for large-scale simulations.

The resulting model encompasses the major hippocampal regions, including the entorhinal cortex (EC), dentate gyrus (DG), CA3, and CA1, with realistic neuronal spiking dynamics, laminar organization, and cell-type composition. Both long-range feedforward pathways and local recurrent circuits are represented, allowing reconstruction of the canonical hippocampal circuit together with its intrinsic microcircuitry.

Consistent with the known trisynaptic organization, inter-regional connectivity includes projections from EC to DG, DG to CA3, and CA3 to CA1, together with direct EC inputs to CA3 and CA1 (**Fig. 2b**). The resulting neuron-type connectivity graph captures all major feedforward projections between hippocampal subregions **(Fig. 2d**). At single-neuron resolution, tracer-derived topographic organization gives rise to structured connectivity maps along the dorsal–ventral axis (**Fig. 2e**). Most projections exhibit diagonal connectivity bands, reflecting topographic organization in which neighboring neurons preferentially connect with neighboring targets, whereas broader bands indicate more spatially diffuse projections.

Within each hippocampal subregion, the framework reconstructs local excitatory, inhibitory, and recurrent connectivity among all major neuronal populations (**Fig. 2f**). The resulting single-neuron connectivity maps reveal that most neuronal populations exhibit

local connectivity concentrated along the diagonal, consistent with a single-peak spatial organization (**Fig. 2g)**. In contrast, dentate gyrus mossy cells display a distinctive bimodal connectivity pattern with two separate connectivity peaks, consistent with their characteristic long-range associational projections[46,47]. Together, these results demonstrate that the framework reconstructs anatomically realistic hippocampal connectivity from the level of neuronal populations to explicit synaptic connections between individual neurons.

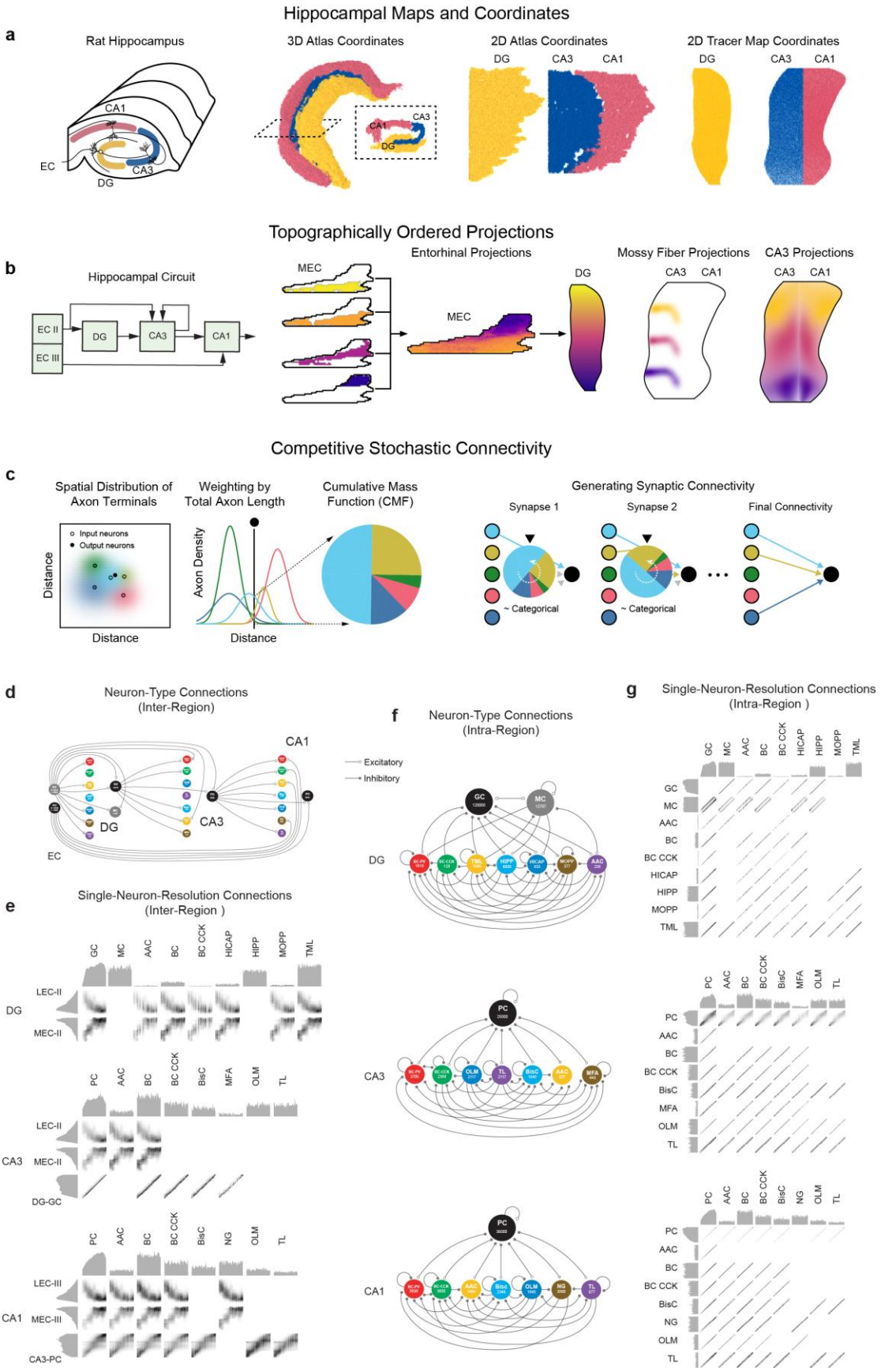

Hippocampal Maps and Coordinates
a
Rat Hippocampus
3D Atlas Coordinates
2D Atlas Coordinates
2D Tracer Map Coordinates
CA1
EC
CA3
DG
Topographically Ordered Projections
b
Hippocampal Circuit
Entorhinal Projections
Mossy Fiber Projections
CA3 Projections
EC II
EC III
MEC
Competitive Stochastic Connectivity
c
Spatial Distribution of Axon Terminals
Weighting by Total Axon Length
Cumulative Mass Function (CMF)
Generating Synaptic Connectivity
Synapse 1
Synapse 2
Final Connectivity
Input neurons
Output neurons
Distance
Axon Density
~ Categorical
d
Neuron-Type Connections (Inter-Region)
e
Single-Neuron-Resolution Connections (Inter-Region)
f
Neuron-Type Connections (Intra-Region)
Excitatory
Inhibitory
g
Single-Neuron-Resolution Connections (Intra-Region)
GC
MC
AAC
BC
BC CCK
HICAP
HIPP
MOPP
TML
PC
BisC
MFA
OLM
NG
TL
LEC-II
MEC-II
LEC-III
MEC-III
DG-GC
CA3-PC

Fig. 2 | Anatomically constrained generation of whole-hippocampus connectivity at single-neuron resolution. a, Anatomical coordinate transformation. Hippocampal subregions are transformed from native three-dimensional atlas coordinates into standardized flattened two-dimensional coordinates, enabling integration of anatomical and tracer-derived projection maps. **b,** Topographically organized axonal projections. The canonical hippocampal circuit and representative tracer-derived projection patterns illustrate the spatial organization of entorhinal, dentate granule cell mossy fiber, and CA3 associational and Schaffer collateral pathways. Anatomical projection maps are parameterized as continuous axonal probability density functions that preserve experimentally observed topography. **c,** Competitive stochastic connectivity generation. For each postsynaptic neuron, presynaptic axonal densities are weighted by axon length and normalized to generate a probability distribution. Synaptic connections are assigned through successive stochastic sampling while respecting anatomical convergence, divergence, and laminar constraints. (**d,f**) Cell-type-specific connectivity. Inter-region (**d**) and intra-region (**f**) connectivity graphs illustrate excitatory and inhibitory projections among neuronal populations in EC, DG, CA3, and CA1. Nodes represent neuronal types, with principal cells shown in black, mossy cells in gray, and interneuron classes color-coded. Directed edges indicate synaptic projections, with open and filled circles denoting excitatory and inhibitory connections, respectively. Numbers within nodes indicate estimated neuronal population sizes. (**e,g**) Single-neuron-resolution connectivity. Inter-region (**e**) and intra-region (**g**) connectivity matrices illustrate anatomically constrained connections among individual neurons in DG, CA3, and CA1. Gray histograms indicate neuronal density distributions along the dorsoventral axis, and grayscale matrices represent spatially organized connectivity between presynaptic and postsynaptic populations. Narrow diagonal bands reflect highly topographic or locally restricted connectivity, whereas broader or multiple bands indicate more spatially distributed projections, including the characteristic bimodal connectivity of dentate mossy cells.

GPU-accelerated platform with electrophysiologically constrained single-neuron properties

To support the simulation of anatomically realistic networks at scale, we implemented the hippocampal model on CARLsim6[48], a GPU-accelerated simulation platform that integrates electrophysiologically constrained neuron and synapse models (**Fig. 1c**). Single neurons were represented using customized nine-parameter Izhikevich formulations[49], which enabled the reproduction of characteristic spiking behaviors while maintaining computational efficiency (**Fig. 1b**). The single-neuron-level connectivity was loaded into the model to connect these neurons to form the large-scale neuronal model of the whole hippocampus. Based on the neuron types and hippocampal subregions, connectivity was realized as either excitatory (AMPA and NMDA) or inhibitory ($GABA_A$ and $GABA_B$) synapses with tunable parameters (**Fig. 1b**).

The model includes 25 distinct neuron types spanning principal neurons and major interneuron classes across DG, CA3, and CA1 (**Figs. 3**). Each neuron type was parameterized to reproduce experimentally recorded firing patterns, resting membrane potentials, instantaneous threshold potential, and adaptation properties. Neurons in the entorhinal cortex were modeled as point processes, consistent with the abstraction level of the present framework and the focus on hippocampal circuit dynamics. Together with conductance-based synapses, the model reproduces physiologically realistic unitary synaptic responses both between hippocampal subregions and within local microcircuits (**Figs. 3**). Although synaptic weights were further refined during network-level optimization, the resulting PSP waveforms remained consistent with experimentally constrained single-neuron responses, preserving biologically realistic synaptic transmission throughout the optimized network.

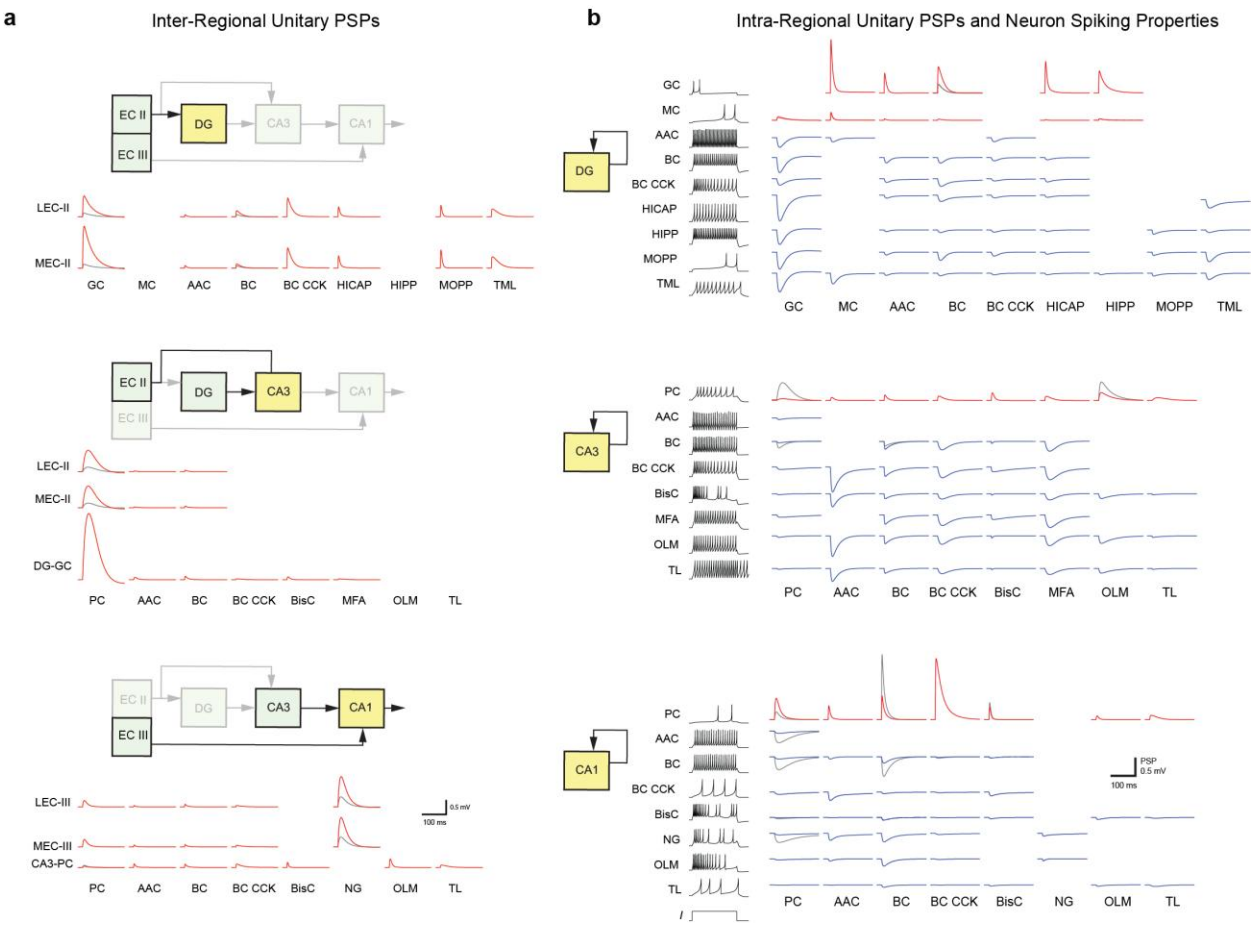


Fig. 3 | Electrophysiologically constrained neuronal spiking properties and unitary postsynaptic potentials across the hippocampal circuit. a, Inter-regional unitary PSPs. Representative postsynaptic responses to single presynaptic spikes across the major feedforward pathways connecting EC, DG, CA3, and CA1. DG neurons receive inputs from layer II neurons of the lateral and medial entorhinal cortex (LEC-II and MEC-II); CA3 neurons receive inputs from EC layer II and DG granule cells (DG-GC); and CA1 neurons receive inputs from EC layer III (LEC-III and MEC-III) and CA3 pyramidal cells (CA3-PC). Circuit schematics highlight the corresponding pathways. **b,** Intra-regional neuronal spiking properties and unitary PSPs. Representative intrinsic firing patterns and synaptic responses among neuronal types within DG, CA3, and CA1. Traces in the leftmost column illustrate cell-type-specific firing patterns evoked by step-current injection, as reproduced by the nine-parameter Izhikevich neuron models. Connectivity matrices show unitary PSPs with presynaptic neuron types arranged in rows and postsynaptic neuron types in columns. In both panels, red and blue traces indicate excitatory (EPSPs)

and inhibitory (IPSPs) postsynaptic potentials, respectively, elicited by a single presynaptic spike. Colored traces represent synaptic responses after network-level optimization, whereas gray traces indicate initial single-neuron-level calibration results for connections with available experimental unitary PSP measurements.

Using this implementation, we simulated a one-tenth-scale hippocampal model comprising approximately 250,000 neurons and 20 million synapses on a single GPU (NVIDIA Quadro RTX 6000,128 GB CPU RAM, 25 GB GPU memory) while preserving the complete anatomical organization of the hippocampus. To estimate the computational resources required across different simulation scales, we quantified the scaling of setup time, the runtime factor (wall-clock execution time divided by simulated biological time, excluding network setup time), and CPU/GPU memory usage as functions of network size. Results show that setup time and CPU/GPU memory usage scaled approximately linearly with network size, with power-law exponents close to 1, whereas the runtime factor exhibited sublinear scaling with an exponent of approximately 0.6 (**Fig. 4a**).

Extrapolation to the full-scale model, based on the neuron count, predicted a setup time of 14,973 s (4.16 h), a runtime factor of 49.9, and memory requirements of 694 GB of CPU RAM and 143 GB of GPU RAM. Independent extrapolation based on synapse count yielded similar estimates: a setup time of 4.17 h, a runtime factor of 50.1, and memory requirements of 711 GB of CPU RAM and 144 GB of GPU RAM. A runtime factor of approximately 50 corresponds to ~16.7 h of wall-clock execution for 20 min of simulated biological activity, excluding network setup. Although these memory requirements exceed the 128 GB of CPU RAM and 25 GB of GPU memory available on the current workstation, they are within the capacity of modern high-memory computing systems, supporting the feasibility of full-scale hippocampal simulations on appropriately configured, potentially multi-GPU, high-memory platforms.

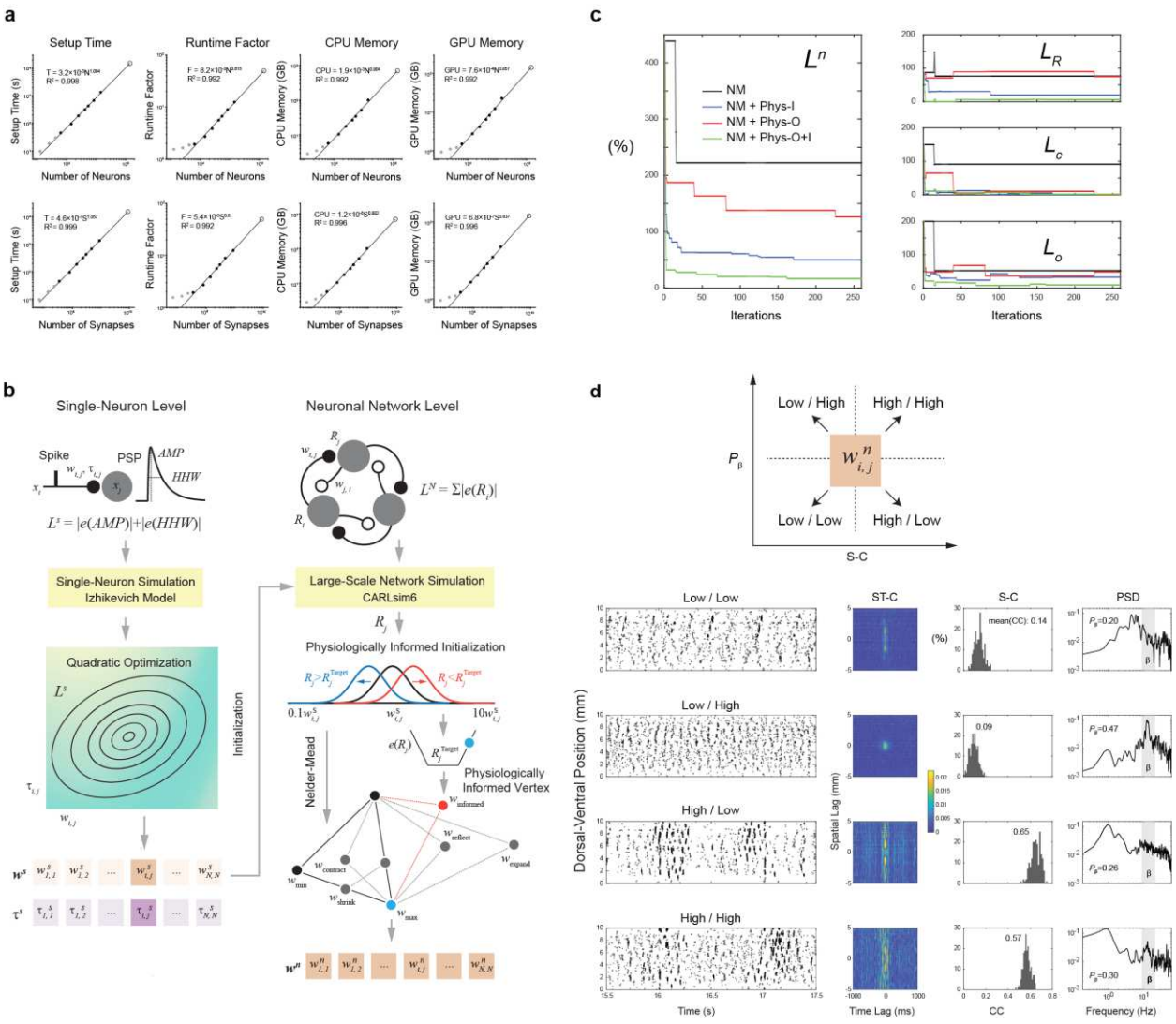


Fig. 4 | Computational scaling and two-stage optimization of the large-scale hippocampal network model. a, Computational scaling. Setup time, runtime factor, CPU memory usage, and GPU memory usage as functions of neuron number (top) and synapse number (bottom). Measurements were obtained from ten progressively scaled DG networks, each simulated for 10 s of biological time. Filled circles indicate measured values (black, included in fitting; gray, excluded), and open circles indicate extrapolated values for the full-scale network (~1.42 million neurons and ~8.84 billion synapses). Gray lines show power-law fits to the seven largest measured networks. Fitted equations and coefficients of determination (R^2) are indicated in each panel. **b,** Two-stage hierarchical optimization. At the single-neuron level (left), synaptic conductance weights and decay time constants are optimized to reproduce experimentally measured unitary PSP

amplitudes (AMP) and half-height widths (HHW). The resulting parameters initialize the large-scale CARLsim6 network simulation (right), where synaptic weights are further optimized against population-level physiological targets while decay time constants remain fixed. Physiologically informed initialization and simplex operations are incorporated into the Nelder–Mead algorithm to accelerate convergence. **c,** Optimization performance. Comparison of conventional Nelder–Mead (NM), NM with physiologically informed initialization (Phys-I), NM with physiologically informed simplex operations (Phys-O), and NM combining both strategies (Phys-O+I). The combined method achieves the fastest convergence and lowest final total loss (L_n), as well as reduced individual losses for mean firing rates (L_R), spatial correlation (L_C), and oscillatory power (L_O). **d,** Multi-objective optimization of network dynamics. Synaptic weights are optimized to produce four target combinations of low or high beta-band power (P_β) and spatial correlation (S-C). Representative results for each target state (Low/Low, Low/High, High/Low, and High/High) show, from left to right, population spike rasters, spatiotemporal correlations (ST-C), spatial correlation distributions (S-C), and power spectral densities (PSD). The optimized networks reproduce distinct combinations of oscillatory power and spatial correlation, demonstrating flexible control of multiple population-level activity features.

Two-stage hierarchical optimization of the large-scale hippocampal model

To calibrate the large-scale hippocampal model while preserving anatomically constrained connectivity, we developed a two-stage hierarchical optimization framework that integrates single-neuron and network-level constraints (**Fig. 4b**). In the first stage, synaptic parameters were optimized using isolated neuron pairs to reproduce experimentally measured unitary PSPs. Synaptic weights and decay time constants were fitted to match both PSP amplitude and temporal profile, establishing physiologically realistic synaptic dynamics for each connection.

These optimized synaptic parameters were then used to initialize the large-scale hippocampal network, where synaptic weights were further refined to reproduce population-level electrophysiological properties, such as the mean firing rates of individual neuronal populations. Unlike conventional approaches that repeatedly restart simulations, synaptic weights were updated online during continuous network simulation, allowing optimization to be performed without disrupting ongoing network activity or re-establishing transient dynamics. This strategy enables efficient fitting of emergent network behavior over behaviorally relevant timescales while preserving biologically realistic single-synapse properties.

To efficiently optimize the high-dimensional parameter space, we developed a physiologically informed Nelder–Mead algorithm that incorporates anatomical and physiological knowledge into both parameter initialization and simplex construction[50] (**Fig. 4b**). Compared with conventional Nelder–Mead optimization[51], physiologically informed initialization or simplex construction alone each improved convergence, whereas combining both strategies produced the fastest convergence and the lowest overall loss across all optimization objectives, including neuronal firing rates, spatial correlation, and oscillatory activity (**Fig. 4c**).

The optimization framework supports simultaneous fitting of multiple emergent network features with minimal additional computational overhead. By specifying different target combinations of beta-band oscillatory power and spatial correlation with the same meaning firing rates, the optimized networks reproducibly converged to distinct activity states while preserving stable circuit dynamics (**Fig. 4d**). These results demonstrate that

the framework can independently and jointly regulate multiple population-level activity features through physiologically constrained optimization of synaptic connectivity.

Taken together, this hierarchical optimization strategy bridges experimentally constrained single-neuron physiology and emergent network dynamics, providing an efficient and scalable approach to calibrating anatomically realistic hippocampal models.

Emergent functional organization and network dynamics

To evaluate whether the anatomically and electrophysiologically constrained model reproduces hippocampal function at behavioral timescales, we simulated virtual spatial exploration in which the network received continuous input from the EC. Medial entorhinal cortex (MEC) neurons provided position-dependent grid-cell activity, whereas lateral entorhinal cortex (LEC) neurons supplied non-spatial contextual input. These anatomically organized inputs drove the complete hippocampal circuit continuously during virtual navigation, allowing network activity to evolve through recurrent interactions over extended simulations[52].

The optimized network generated rich spatiotemporal firing patterns across all hippocampal subregions. Population raster plots revealed coordinated activity among principal neurons and interneurons in the DG, CA3, and CA1, with distinct firing statistics emerging for each neuronal population (**Fig. 5a**). Quantitative analyses further showed neuron-type-specific firing-rate distributions, spatiotemporal correlation structures, and PSDs, demonstrating diverse yet highly organized population dynamics across the hippocampal circuit. Oscillatory activity emerged naturally in the theta and gamma frequency bands through interactions between excitatory and inhibitory populations, providing an additional physiological validation of the network dynamics.

Beyond reproducing population activity, the model generated physiologically realistic spatial representations. Without imposing explicit spatial tuning or place-field constraints, stable place-selective firing emerged spontaneously throughout the hippocampal circuit from anatomically constrained connectivity, experimentally calibrated neuronal and synaptic properties, and ongoing network interactions (**Fig. 5b**). Spatial representations transformed progressively across hippocampal subregions. EC neurons exhibited multiple grid-like spatial firing fields as designed, whereas DG granule cells frequently

developed multiple discrete place fields. In contrast, CA3 and CA1 pyramidal neurons predominantly exhibited single, spatially localized place fields, consistent with experimental observations of spatial coding along the trisynaptic pathway[53]. Quantitatively, spatial information increased progressively from EC through DG and CA3 to CA1 (**Fig. 5c**), indicating increasingly informative spatial representations along the hippocampal circuit. This transformation emerged without explicit place-field tuning, suggesting that anatomically organized connectivity and neuronal dynamics can support the progressive refinement of spatial coding. These place fields remained stable throughout extended simulations, demonstrating that the model preserves coherent spatial coding over behavioral timescales.

Together, these results demonstrate that the framework reproduces both the physiological dynamics and functional organization of the hippocampus at the scale of the entire circuit. The emergence of coordinated population dynamics, physiologically relevant oscillatory activity, and stable spatial representations from anatomically constrained connectivity and electrophysiologically calibrated neuronal models establishes the framework as a platform for investigating the circuit mechanisms underlying spatial navigation and other hippocampus-dependent functions over behaviorally relevant timescales.

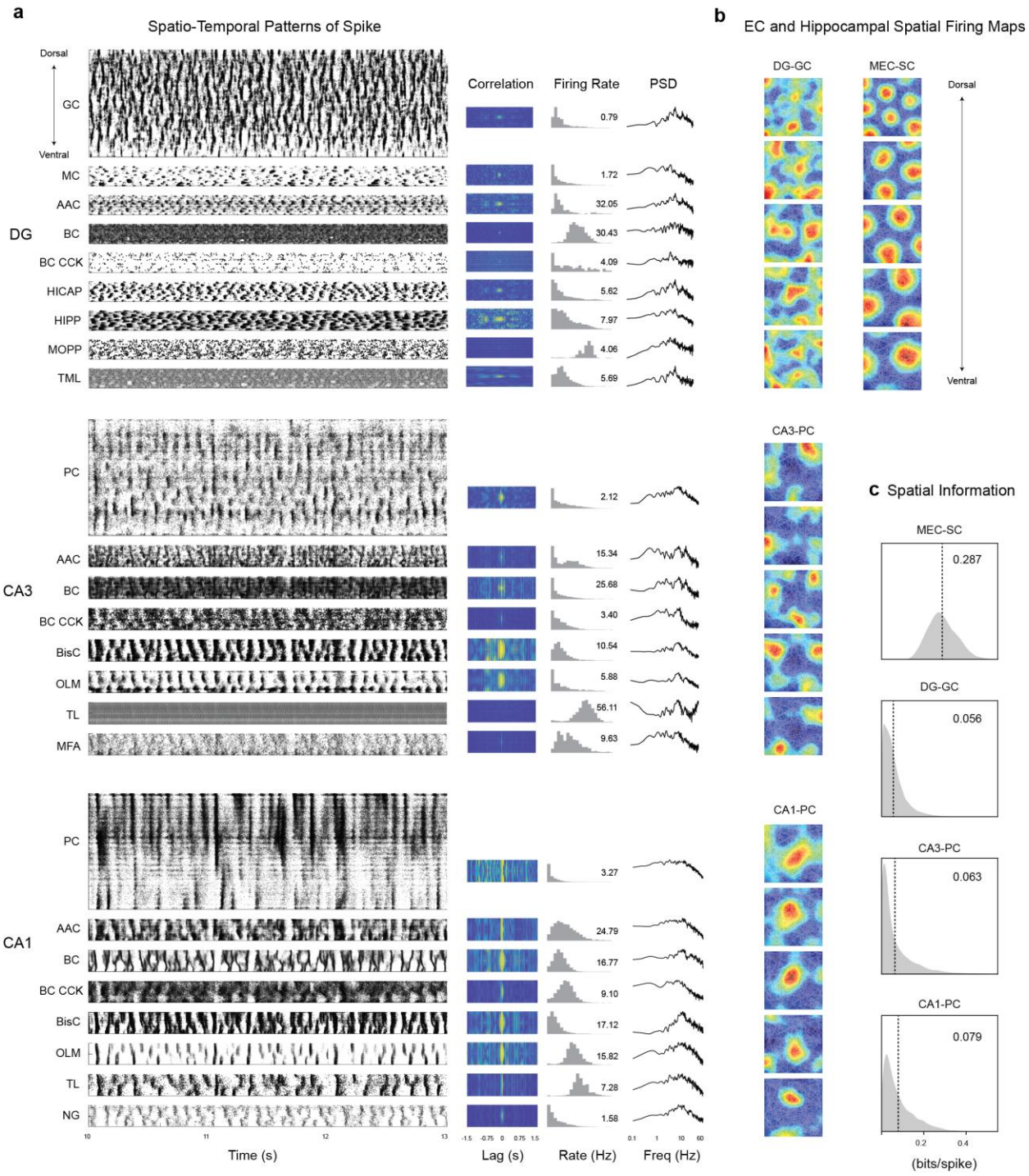


Fig. 5 | Emergent network dynamics and spatial representations across the hippocampal circuit during virtual navigation. a, Spatiotemporal network activity. Representative spike rasters (3-s duration) for neuronal populations in DG, CA3, and CA1, with neurons ordered along the dorsoventral axis. Each dot represents an action potential. Corresponding panels show spatiotemporal correlations of population spiking activity,

distributions of neuronal mean firing rates (with population means indicated), and power spectral densities (PSD), illustrating cell-type-specific firing statistics, coordinated activity, and oscillatory dynamics. **b,** Spatial firing maps. Representative spatial firing maps of five neurons from each population, medial entorhinal cortex stellate cells (MEC-SC), DG granule cells (DG-GC), CA3 pyramidal cells (CA3-PC), and CA1 pyramidal cells (CA1-PC), sampled across the dorsoventral axis. Maps were reconstructed from spike trains and virtual-animal trajectories in a 60 × 60 cm arena using 4 × 4 cm spatial bins and Gaussian smoothing (σ = 3 cm). Maps were independently normalized and color-scaled, with warmer colors indicating higher relative firing rates. MEC grid fields were prescribed by the input model, whereas hippocampal spatial firing patterns emerged without explicit place-field tuning. MEC neurons exhibit multiple grid-like firing fields, DG granule cells frequently display multiple spatial fields, and CA3 and CA1 pyramidal neurons exhibit more spatially localized firing patterns. **c,** Spatial information . Population distributions of spatial information (bits/spike) for MEC-SC, DG-GC, CA3-PC, and CA1-PC neurons. Dashed vertical lines and numerical values indicate population means.

Comparison with existing large-scale network models

Having demonstrated anatomically constrained connectivity, electrophysiologically calibrated neuronal dynamics, efficient large-scale simulation, and emergent hippocampal activity, we compared the capabilities and computational performance of our framework with representative large-scale neuronal network models implemented using CPU- and GPU-based simulators (**Table 1**). Because these models differ in network size, neuronal complexity, numerical methods, and hardware, direct performance comparisons are limited. We therefore evaluated both computational efficiency and biological modeling capabilities, with detailed benchmark information provided in **Supplementary Table 1**.

Existing CPU-based platforms, including NEST and CoreNEURON, support large networks with anatomically constrained connectivity and, in some implementations, morphologically detailed neuronal models[54,55]. However, the representative models considered here required substantial computational resources, with reported runtime factors ranging from approximately 50,000 to 2 million. GPU-based platforms, including NEST GPU and Brian2CUDA, achieve substantially greater computational efficiency, supporting simulations of millions of neurons with runtime factors of approximately 50–200, although the compared implementations generally employ simplified neuronal representations[56,57]. After normalization for GPU double-precision performance, our full-scale hippocampal model yielded an estimated adjusted runtime factor of 134, compared with 213 and 199 for the representative GPU-based models. Although these values do not constitute a controlled benchmark, they suggest that the present framework achieves competitive computational efficiency while incorporating anatomically constrained single-neuron connectivity and electrophysiologically calibrated neuronal and synaptic dynamics.

An additional advantage of the framework is its support for online parameter optimization. Network initialization can impose substantial computational overhead in large-scale simulations, particularly when repeated across hundreds of optimization iterations. By updating synaptic parameters during continuous simulation, CARLsim6 avoids repeated network initialization and enables efficient optimization of emergent network dynamics. Together, these capabilities provide a practical balance between biological realism,

computational scalability, and functional optimization over behaviorally relevant timescales.

Table 1: Comparison of Large-Scale Neuronal Network Models Across Simulators

Model	Rat Hippocampal DG–CA3–CA1		Macaque Visual System	Excitatory/ Inhibitory Network	Human Hippocampal CA1	Rat Hippocampal CA1
Publication	This Study		Tiddia et al., 2022	Alevi et al., 2022	Gandolfi et al., 2023	Romani et al., 2024
Simulator	CARLsim6		NEST GPU	Brian2CUDA	NEST	CoreNEURON
Hardware	GPU		GPU	GPU	CPU	CPU
Number of Neurons	240,000	1,900,000	4,100,000	320,000	5,280,000	470,000
Setup Time (minutes)	74	966	16	4	23	N/A
Adjusted Runtime Factor	48	134	213	199	54,270	2,244,648
Anatomically Constrained Connectivity	✓	✓	×	×	✓	✓
Electrophysiologically Constrained Neuron Models	✓	✓	×	×	✓	✓
Morphologically Realistic Neuron Models	×	×	×	×	×	✓
Behavioral-Timescale Simulation	✓	✓	✓	✓	×	×
Online Optimization	✓	✓	×	×	×	×

Discussion

We present a computational framework for constructing and simulating large-scale spiking neural networks with single-neuron-level connectivity constrained by multiscale anatomical and electrophysiological data. Applied to the hippocampus, the framework integrates cell-type composition, spatial distributions, laminar organization, topographically organized projections, neuronal electrophysiology, and synaptic dynamics within a unified model. When driven by behaviorally relevant inputs, the network generates population dynamics and spatial representations characteristic of *in vivo* hippocampal activity. The framework therefore provides a bridge between increasingly detailed structural descriptions of neural circuits and their emergent function during behavior.

This capability is particularly relevant as large-scale efforts such as the BRAIN Initiative Cell Census Network (BICCN) generate increasingly comprehensive descriptions of neuronal cell types, spatial organization, connectivity, and molecular and electrophysiological properties[58]. Studies integrating gene expression and anatomical connectivity have further revealed the multiscale organization and functional heterogeneity of hippocampal networks[41–43]. Complementary efforts, such as Hippocampome.org, have systematically characterized hippocampal neuron types and their morphological, molecular, and electrophysiological properties, highlighting the importance of axonal and dendritic organization in defining neuronal identities and circuit connectivity[44,45,59]. Our framework builds on these advances by integrating heterogeneous anatomical and physiological measurements into explicit, single-neuron-resolution network models, enabling the functional consequences of spatially organized circuit architecture to be investigated directly.

A key result is that biologically relevant network dynamics emerge without being explicitly prescribed at the level of individual hippocampal neurons. Behaviorally structured entorhinal input is progressively transformed across DG, CA3, and CA1, producing spatially selective hippocampal activity. Thus, spatial representations arise from interactions among structured input, anatomically organized connectivity, intrinsic neuronal dynamics, and recurrent circuitry rather than from explicitly assigned place fields.

This provides a functional test of whether anatomical and electrophysiological constraints assembled primarily from lower-level experiments can collectively generate network properties observed during behavior.

A major challenge in biologically realistic network modeling is balancing anatomical and electrophysiological detail with computational efficiency. Existing large-scale models span a wide range of biological complexity and computational performance, with detailed CPU-based models often requiring substantial computing resources and GPU-based approaches achieving greater efficiency through simplified neuronal representations. Our framework helps bridge this gap by combining anatomically constrained single-neuron connectivity and electrophysiologically calibrated neuronal dynamics with GPU-accelerated simulation over behaviorally relevant timescales. Importantly, computational scalability not only enables longer simulations but also makes iterative optimization of large mechanistic networks increasingly practical.

Conventional bottom-up modeling constrains neuronal and synaptic parameters using measurements at corresponding biological scales, but reproducing these local properties does not guarantee realistic population dynamics. Our two-stage framework addresses this limitation by combining bottom-up calibration of unitary synaptic responses with top-down optimization against population firing rates, correlations, and oscillatory activity. Together with online parameter updating, this approach enables large-scale mechanistic networks to be optimized directly against emergent functional properties while preserving experimentally constrained anatomical organization. More broadly, the same strategy could incorporate spatial tuning, neural population trajectories, and behavioral performance as additional functional constraints, providing a systematic means of linking cellular and circuit mechanisms to higher-level brain function.

The ability to simulate and optimize biologically constrained networks at scale also creates opportunities for integration with data-driven machine-learning and AI approaches. These methods are powerful tools for extracting structure from high-dimensional neural data and predicting neural activity or behavior[60–62], but predictive accuracy alone does not necessarily reveal the underlying neuronal, synaptic, and circuit mechanisms. Mechanistic models provide a complementary approach by explicitly

representing biological components and their interactions, allowing emergent network properties to be investigated through targeted perturbations and sensitivity analyses.

The two approaches are therefore complementary rather than competing[38,39,63,64]. AI methods could help estimate poorly constrained parameters, identify structure in neural activity, and accelerate optimization, whereas biologically constrained network models can provide mechanistic priors and interpretable substrates for hypothesis testing. Their integration offers a potential route toward models combining the predictive capabilities of AI with the biological interpretability of mechanistic neuroscience.

Several limitations define priorities for future development. First, neurons are represented using single-compartment Izhikevich models, which efficiently reproduce diverse firing phenotypes but do not capture spatially distributed and nonlinear dendritic computations. This is particularly relevant in CA1, where entorhinal and CA3 inputs target distinct dendritic domains. Reduced multi-compartment models could capture key aspects of dendritic integration while remaining computationally tractable and could additionally support more biophysically grounded calculations of dipoles and local field potentials[65].

Second, the model is not yet anatomically complete. The current implementation includes MEC, LEC, DG, CA3, and CA1 together with major feedforward pathways and extensive intra-subfield circuitry but does not include CA2 and several inter-subfield and feedback projections. Future extensions should also incorporate additional functional populations in MEC and LEC, inputs from other brain regions, and experimentally constrained synaptic plasticity to address learning, remapping, memory formation, and consolidation.

Finally, network-level optimization does not necessarily identify a unique set of microscopic parameters. Different combinations of synaptic strengths may produce similar population dynamics, and optimized parameters should therefore be interpreted as configurations consistent with the imposed anatomical, electrophysiological, and functional constraints rather than direct estimates of biological synaptic strengths. Sensitivity analyses, targeted perturbations, and validation against independent experimental measurements will be important for identifying robust mechanistic predictions.

Despite these limitations, the framework establishes a scalable foundation for integrating anatomical structure, cellular and synaptic physiology, network dynamics, and behavior within a common computational model. As more comprehensive experimental data become available, iterative integration of experimental constraints, large-scale simulations, optimization, and model-driven predictions can progressively yield more complete and experimentally testable models of hippocampal circuit function.

Methods

We developed an anatomically constrained, large-scale spiking network model of the hippocampus that integrates multiscale anatomical data with electrophysiologically grounded neuronal and synaptic dynamics (**Fig. 1**). This section describes the construction of the spatial framework, neuron placement, and connectivity generation, as well as the neuron and synapse models used to simulate hippocampal activity. We further detail the optimization procedures used to align model dynamics with experimental constraints, as well as the GPU-accelerated simulation platform that enables long-duration, large-scale simulations, and optimization. Together, these methods establish a reproducible framework for modeling the whole hippocampus at single-neuron resolution and behaviorally relevant timescales.

Spatial framework and coordinate systems

The hippocampus exhibits a highly curved and interlocked three-dimensional anatomy, with substantial anatomical and molecular heterogeneity along its longitudinal and transverse axes. This spatial organization underlies distinct connectivity patterns and functional specialization across hippocampal subregions[41–43]. To preserve this organization while facilitating spatial modeling and connectivity analysis, we adopted a flattened hippocampal coordinate system widely used to characterize anatomical and connectivity gradients[66,67]. In this representation, hippocampal subfields are unfolded into a two-dimensional plane, while laminar organization is preserved along the third spatial dimension (**Fig. 2a**). Thus, the flattened representation retains the model's three-dimensional anatomical organization while providing an interpretable coordinate system that can be mapped back to the native hippocampal geometry.

Mapping between flattened and anatomical coordinates was generated using the Ropireddi hippocampus atlas[68], which provides longitudinal and transverse coordinates for three-dimensional hippocampal space. Interpolation was used to construct a continuous transformation between flattened and unflattened representations, enabling all neurons and synaptic connections to be defined in flattened space while retaining the ability to visualize and analyze results in anatomical coordinates (**Fig. 2b**).

In the flattened coordinate system, the longitudinal axis, also referred to as the septo-temporal or dorso-ventral axis, corresponds to the primary axis along the length of the hippocampus and is represented as the y-axis in figures. The transverse axis, represented as the x-axis, is perpendicular to the longitudinal axis and spans hippocampal subfields in the following order: the infrapyramidal and suprapyramidal blades of DG, CA3c, CA3b, CA3a, and proximal and distal CA1. Anatomical boundaries for each subfield were derived from published flattened maps of the hippocampus and entorhinal cortex (**Supplementary Table 2**).

The EC, which lies outside the hippocampus proper, was modeled using a separate, flattened coordinate system that reflects its distinct anatomy and topographic organization. Flattened maps for the medial and lateral entorhinal cortices (MEC and LEC) were obtained from Dolorfo and Amaral[69] and preserve the dorsoventral and mediolateral axes known to underlie topographic hippocampal input.

Flattened maps for the dentate gyrus were derived from Gaarskjaer[70], which quantified the widths of the infrapyramidal and suprapyramidal blades relative to the crest at successive longitudinal positions. Flattened maps for CA3 and CA1 were derived from Ishizuka et al[71], which presented tracer-based connectivity data across multiple animals in a consistent flattened coordinate system encompassing CA1, CA2, and CA3. Boundary coordinates for all subfields were obtained by digitizing published figures and applying reported scale bars.

Neuron placement

Neuron placement was defined independently for each cell type by specifying both the total number of neurons and their spatial distribution within the corresponding hippocampal subfields. Spatial distributions were defined based on somatic location and could vary along the longitudinal and transverse axes, although experimentally measured density profiles are most commonly available along the longitudinal axis. Accordingly, longitudinal density gradients were used as the primary constraint for neuron placement, with transverse distributions assumed to be uniform within subfield boundaries unless otherwise reported.

For principal neurons, total cell counts and detailed longitudinal density profiles are well established and incorporated directly from the literature[72]. For GABAergic interneurons, total neuron counts were estimated using marker-based cell counts, with chemical marker expression used to assign putative interneuron identities. See **Supplemental Table 3** for a list of all cell counts. Where available, studies reporting lamina-specific distributions of interneurons were used to further partition total counts across hippocampal layers. In cases where only coarse dorsal–ventral distributions were reported, these measurements were used to constrain longitudinal placement.

Somatic positions were generated using a rejection-sampling (thinning) procedure. Experimentally measured somatic density profiles were normalized to define probability density functions along the longitudinal axis. Candidate longitudinal positions were drawn from a uniform distribution and accepted or rejected based on the local probability defined by the normalized density. This process was repeated until the required number of neurons for each cell type was obtained.

For each accepted longitudinal position, the transverse coordinate was sampled uniformly within the anatomical boundaries of the corresponding subfield. Laminar positions were then assigned according to cell-type–specific layer distributions, ensuring that neurons were placed only within anatomically appropriate layers. Together, this procedure ensured that neuron placement respected experimentally observed density gradients while maintaining flexibility in regions where detailed spatial measurements are unavailable.

Single-neuron level connectivity generation

Synaptic connectivity was generated using an anatomically constrained, stochastic framework that integrates spatial organization, axonal projection patterns, and cell-type–specific synaptic statistics. Connectivity was instantiated at single-neuron resolution, such that each synaptic connection was defined explicitly between individual presynaptic and postsynaptic neurons. The procedure combines convergence and divergence constraints with spatially defined axonal probability density functions (PDFs) to produce biologically realistic wiring patterns across hippocampal subfields and laminae (**Fig. 2c**).

Convergence and divergence constraints

Synaptic connectivity was constrained using experimentally derived estimates of synaptic convergence (the number of inputs per neuron) and, where available, divergence (the number of outputs per neuron). Convergence for excitatory inputs was estimated from measurements of total dendritic length and spine density[73] , using lamina-specific values when reported (**Supplemental Tables 4-12**). These measurements were used to compute the number of excitatory synapses allocated to each postsynaptic neuron, partitioned across laminae according to dendritic distribution.

Inhibitory convergence was estimated based on the synaptic density of GABAergic synapses where available[74,75], or else using bulk tissue measurements of excitatory-to-inhibitory synapse ratios, allowing inhibitory synapse counts to be inferred from excitatory spine estimates[76] (**Supplemental Tables 13-15**). Lamina-specific inhibitory distributions were incorporated to restrict inhibitory synapses to anatomically appropriate layers. Divergence constraints based on axon bouton counts were applied selectively, as full axonal reconstructions are limited for most hippocampal cell types. An important exception was the dentate granule cell mossy fiber projection to CA3, for which divergence estimates are well characterized and were applied explicitly[77].

A convergence-based formulation was used for most projections, ensuring that synaptic input density per neuron was preserved under network scaling. This approach allows reduced-scale models to retain biologically meaningful synaptic statistics while supporting systematic expansion to larger network sizes.

Axonal probability density functions

Axonal PDFs were defined to capture both the spatial extent and topographic organization of presynaptic projections.

For intra-subfield projections, axonal distributions were typically centered on the presynaptic soma, reflecting locally distributed arborizations. These distributions were parameterized using Gaussian functions fitted to the reported axon density measurements or estimates of axonal extent (**Fig. 2c, Supplemental Tables 16 and 17**).

For inter-subfield projections, axonal PDFs incorporated experimentally observed topographic gradients derived from tracer injection studies. In these cases, the location parameters of the PDFs varied as a function of presynaptic position, while shape parameters (e.g., variance and skew) captured the spatial spread of axon terminals (**Fig. 1a**). Skew-normal distributions were used for projections such as CA3 associational and Schaffer collateral pathways, with parameters fitted to tracer-derived projection maps and interpolated across the presynaptic population. Axonal PDFs were further restricted to laminae in which synaptic contacts have been experimentally observed.

Standardization of tracer-derived projection maps

Tracer injection studies were used to constrain both the topographic organization and spatial extent of inter-subfield projections. Because individual tracer studies were conducted across multiple animals and reported using heterogeneous coordinate systems, all tracer-derived maps were transformed into a standardized flattened reference space (**Fig. 2a**). Subject-specific maps were aligned and averaged where appropriate to define population-level projection profiles and then mapped back into anatomical coordinates for implementation in the model. This procedure ensured consistency across datasets while preserving experimentally observed gradients and projection asymmetries.

Axon distribution parameterization

For each inter-subfield projection, axonal terminal fields were parameterized using two-dimensional, rotated skew-normal PDFs to capture both spatial extent and topographic organization (**Fig. 2b**). Tracer-derived labeling maps were first converted into a standardized square coordinate space to enable consistent parameter estimation across studies. Within this standard space, published tracer data were discretized into three qualitative levels: no labeling, low-density labeling, and high-density labeling. To enable quantitative fitting, numerical values between 1 and 10 were assigned to the low- and high-density labels, with the high-density values constrained to exceed the low-density values. Model parameters were optimized in the standardized space and subsequently mapped back into anatomical, subject-specific coordinates for network instantiation.

The skew-normal formulation extends the Gaussian distribution by introducing asymmetry, enabling the representation of nonuniform and directionally biased axonal terminal fields. The standard normal probability density function and its cumulative distribution are defined as

$$\phi(x) = \frac{1}{\sqrt{2\pi}} e^{-\frac{x^2}{2}}$$

$$\Phi(x) = \frac{1}{2}\left[1 + erf\left(\frac{x}{\sqrt{2}}\right)\right]$$

where $erf(\cdot)$ denotes the Gaussian error function. The one-dimensional skew-normal PDF is given by

$$f(x) = \frac{2}{\omega}\phi\left(\frac{x-\xi}{\omega}\right)\Phi\left(\alpha\left(\frac{x-\xi}{\omega}\right)\right)$$

where ξ is the location parameter, ω is the scale (variance) parameter, and α controls the degree and direction of skewness.

To model orientation-dependent axonal projections, the coordinate system was rotated by an angle θ according to

$x' = x \cdot \cos(\theta) + y \cdot \sin(\theta)$, $y' = -x \cdot \sin(\theta) + y \cdot \cos(\theta)$

Using the rotated coordinates, the two-dimensional skew-normal PDF was defined as

$$f(x,y) = \frac{4}{\omega_x \omega_y}\phi\left(\frac{x'-\xi_x}{\omega_x}\right)\Phi\left(\alpha_y\left(\frac{x'-\xi_x}{\omega_x}\right)\right)\phi\left(\frac{y'-\xi_y}{\omega_y}\right)\Phi\left(\alpha_y\left(\frac{y'-\xi_y}{\omega_y}\right)\right)$$

where x and y correspond to transverse and longitudinal positions in the flattened hippocampal coordinate system, respectively. Parameters (ξ_x, ξ_y) specify the center of the axonal terminal field, (ω_x, ω_y) control spatial spread along each axis, (α_x, α_y) control directional skew, and θdetermines orientation.

For CA3 associational and CA3–CA1 Schaffer collateral projections, tracer data from Ishizuka et al provided measurements from nine injection sites arranged in an approximately 3 × 3 grid across the longitudinal and transverse extent of CA3[71]. To define

continuous projection topography across the full region, skew-normal parameters were interpolated across presynaptic positions using cubic splines (**Fig. 1a, 2b**). Where necessary, parameters were extrapolated toward anatomical boundaries by extending the instaneous slope. In cases where this approach yielded implausible parameter values (e.g., excessively small or large variances), the slope magnitude was progressively reduced until the boundary distributions exhibited smooth, biologically plausible transformations. This interpolation–extrapolation procedure was applied consistently to both CA3–CA3 associational projections and CA3–CA1 Schaffer collateral projections.

Stochastic, competitive connectivity assignment

Synaptic connections were generated using a stochastic, competitive sampling procedure driven by spatially defined axonal PDFs. For each postsynaptic neuron and synaptic group (defined by presynaptic cell type and target lamina), axonal densities from all valid presynaptic neurons were computed at the postsynaptic location. These densities were weighted by presynaptic axon length (**Supplemental Tables 18-20**) and normalized to construct a probability mass function (**Fig. 2c**).

Presynaptic neurons were then sampled from this distribution with replacement until all synapses allocated to the postsynaptic neuron were assigned an input (**Fig. 2c**). If divergence constraints were present, presynaptic neurons were removed from future sampling once their output limits were reached. This competitive process ensured that synapses were distributed according to anatomical axon density while respecting cell-type–specific convergence and divergence constraints.

Pathway-specific implementations of connectivity

The network architecture was organized around the classic trisynaptic pathway, consisting of projections from the EC stellate cells to DG granule cells, from DG granule cells to CA3 pyramidal neurons, and from CA3 pyramidal neurons to CA1 pyramidal neurons (**Fig. 2b**). This feedforward scaffold provides a well-characterized anatomical backbone for hippocampal information processing, serving as the initial framework for inter-subfield connectivity. In addition to feedforward pathways, recurrent and feedback projections within subfields were included where supported by anatomical data, enabling internally generated network dynamics.

EC projections to DG and CA3

Projections from the EC to the dentate gyrus and CA3 were modeled based on retrograde tracer studies that revealed spatially restricted terminal fields and strong topographic organization along the longitudinal axis[78]. Axonal terminal fields were parameterized using Gaussian distributions, with standard deviations derived from reported longitudinal spreads (1–1.5 mm) of labeled axons[78]. Transverse distributions were assumed to be uniform within anatomically defined target regions. Laminar targeting was restricted to layers known to receive entorhinal input, and conduction delays were assigned based on estimated axonal path lengths.

DG mossy fiber projections to CA3

Projections from dentate granule cells to CA3 pyramidal neurons were modeled as mossy fiber pathways, which are characterized by sparse connectivity and relatively simple axonal morphology, i.e., few or no collaterals[66]. Due to the availability of bouton count estimates and the limited branching of mossy fibers, these projections were constrained using divergence-based rules rather than convergence alone. Axonal trajectories were modeled explicitly to capture the curved path of mossy fibers within the CA3 region, and synaptic contacts were restricted to experimentally observed target layers (**Fig. 2b**). Mossy fibers originating from infrapyramidal granule cells were restricted to the stratum oriens proximal to the soma in CA3c before crossing into the stratum lucidum in CA3b and CA3a. Mossy fibers of suprapyramidal origin remained in the stratum lucidum for the entire transverse CA3 extent. Mossy fibers did not extend into CA1.

CA3 associational and Schaffer collateral projections

Associational projections within CA3 and Schaffer collateral projections from CA3 to CA1 were parameterized using anterograde tracer studies that revealed pronounced longitudinal topography and asymmetric terminal field distributions[71]. Axonal terminal fields for these pathways were modeled using skew-normal PDFs, allowing directional bias and nonuniform spatial spread to be captured. Distribution parameters were fitted to tracer-derived projection profiles and interpolated across presynaptic positions. Where tracer sampling was sparse, extrapolation was applied cautiously to extend projection fields to anatomical boundaries while maintaining smooth transitions and biologically

plausible distributions. Associational and Schaffer collateral terminals are found in both the stratum radiatum and stratum oriens, and their axonal weightings were derived from the ratio of lengths measured between these strata[79]. Laminar targeting and conduction delays were assigned according to pathway-specific anatomical constraints.

Axonal conduction delays

Axonal conduction delays were assigned based on anatomical path length and conduction velocity (**Supplemental Table 21**). For most projections, path lengths were computed using the Euclidean distance between presynaptic and postsynaptic somata in the 2D flattened space. For dentate granule cell mossy fiber projections, which follow highly curved trajectories, axonal arc length was used to estimate path length more accurately. Axonal conduction delays were then computed by dividing path length by cell-type–specific conduction velocities.

Neuron and synapse models

Neuronal and synaptic dynamics were modeled using computationally efficient, biophysically grounded Izhikevich formulations suitable for large-scale spiking network simulations[49]. All neuron and synapse models were implemented uniformly across hippocampal subfields, with cell-type–specific parameters used to capture physiological diversity while maintaining tractable simulation performance.

Spiking neuron model

Neuronal spiking dynamics were modeled using the nine-parameter Izhikevich neuron model[49], a computationally efficient formulation that captures diverse electrophysiological firing patterns while retaining biophysical interpretability (**Figs. 1b**). The membrane potential v and recovery variable u evolve according to

$$\frac{dv}{dt} = \frac{1}{C}[k(v - v_r)(v - v_t) - u + I]$$

$$\frac{du}{dt} = a\,[b(v - v_r) - u],$$

where C is the membrane capacitance, I is the input current, v_r is the resting membrane potential, v_t is the instantaneous threshold potential, and a, b, and k control the time

scale and sensitivity of the recovery dynamics. When the membrane potential reaches a peak value v_{peak}, a spike is emitted, and the state variables are reset according to

$v \leftarrow c, u \leftarrow u + d$,where c is the reset membrane potential and d determines the post-spike recovery increment. Together, the nine parameters $(a, b, c, d, k, v_r, v_t, v_{\text{peak}}, C)$ define neuronal excitability, spike initiation, and post-spike dynamics.

This extended formulation enables direct tuning of membrane capacitance, resting membrane potentials, instantaneous threshold potential, and adaptation properties, allowing the model to reproduce experimentally measured excitability and firing behaviors while remaining computationally tractable for large-scale network simulations. The model incorporates 25 distinct neuron types across DG, CA3, and CA1. Cell-type classifications and baseline electrophysiological parameters were obtained from Hippocampome.org, a systematically curated knowledge base integrating morphological, molecular, and electrophysiological properties of hippocampal neurons[44,45]. The nine-parameter Izhikevich models were adopted from this resource and refined where necessary to reproduce cell-type-specific electrophysiological targets and ensure stable responses when coupled to conductance-based synapses (**Supplementary Table 22**).

Conductance-based synapse models

Synaptic transmission was modeled using conductance-based (COBA) synapses for excitatory AMPA and NMDA receptors and inhibitory $GABA_A$ and $GABA_B$ receptors (**Fig. 1b**). For AMPA, $GABA_A$, and $GABA_B$ receptor synapses, activation of a presynaptic spike produced a transient change in synaptic conductance modeled as a single decaying exponential[80],

$$g_{\text{syn}}(t) = \sum_f \exp\left(-\frac{t - t_f}{\tau_{\text{syn}}}\right) \Theta(t - t_f)$$

where t_f denotes the arrival time of the presynaptic spike, τ_{syn} is the receptor-specific decay time constant, and $\Theta(\cdot)$ is the Heaviside step function. The corresponding postsynaptic current was computed as

$$i_{\text{syn}}(t) = g_{\text{syn}}(t)\,[v(t) - v_{\text{syn}}^{\text{rev}}],$$

where $v(t)$ is the postsynaptic membrane potential and $v_{\mathrm{syn}}^{\mathrm{rev}}$ is the receptor-specific reversal potential.

NMDA receptor currents were modulated by a voltage-dependent magnesium block[81]. Rather than using the original exponential formulation[82], we employed a computationally efficient Hill-type approximation that preserves the sigmoidal voltage dependence while reducing computational cost during large-scale network simulation.

$$i_{\mathrm{NMDA}} = g_{\mathrm{NMDA}} B_{\mathrm{Mg}}(v)(v - v_{\mathrm{NMDA}}^{\mathrm{rev}})$$

$$B_{\mathrm{Mg}}(v) = \left(\frac{v+80}{60}\right)^2 \Big/ \left[1 + \left(\frac{v+80}{60}\right)^2\right]$$

Synaptic weights $w_{i,j}$ (in nS) scaled the effective conductance from the presynaptic neuron i to the postsynaptic neuron j. The total synaptic current received by neuron j was computed as the weighted sum over all presynaptic inputs, as $I_j = \sum_i i_{ij} w_{ij}$.

This formulation enabled the incorporation of heterogeneous synaptic dynamics and receptor-specific kinetics while maintaining compatibility with large-scale, GPU-accelerated simulations.

Behavioral inputs to the hippocampal network

The MEC and LEC provide the primary cortical inputs to the hippocampus, conveying complementary information streams. Neurons in the MEC primarily encode spatial variables and path-integration signals that support representations of self-location, whereas LEC neurons are less spatially tuned and instead sensitive to non-spatial contextual features, including objects, odors, and temporal associations. In the present model, these distinct functional roles were reflected by implementing structured, location-dependent spatial inputs from MEC and location-independent random inputs from LEC.

<u>Grid-cell–based MEC input</u>

Spatial input from MEC was modeled using grid cells, one of the most extensively characterized entorhinal cell types. Grid cells exhibit spatially periodic firing fields arranged in a triangular lattice that tiles the environment (**Fig. 5b**).

Grid cell model

To model the receptive fields of grid cells, we adopted the formulation introduced by Blair et al[83], in which the grid map is defined as the sum of three cosine gratings rotated by 60° increments[83]:

$$G(\lambda, \theta, \boldsymbol{x}, \boldsymbol{c}) = g\left(\sum_{k=0}^{2} \cos\left(\frac{4\pi}{\lambda\sqrt{3}} * \boldsymbol{R}\left(\theta + \frac{k\pi}{3}\right) \cdot (\boldsymbol{x} - \boldsymbol{c})\right)\right)$$

where $x$denotes the animal's position, c is the spatial offset defining the grid origin, λ is the grid spacing (in cm), and θ is the grid orientation. The rotation matrix is given by

$$\boldsymbol{R}(\theta) = \begin{bmatrix} cos(\theta) \\ sin(\theta) \end{bmatrix}$$

The gain function $g(\cdot)$ ensures non-negative firing rates and was defined as

$$g(x) = e^{a(x-b)} - 1$$

with parameters $a = 0.3$ and $b = -3/2$. The resulting grid-map output was normalized such that the peak firing rate was 50 Hz.

Grid-cell parameters were anatomically constrained based on experimental observations. Hafting et al reported linear relationships between grid spacing, grid field area, and dorso-ventral position within MEC[2], while Stensola et al identified a systematic relationship between grid spacing and grid orientation[84]. These empirical relationships were incorporated via linear regressions to assign grid-map parameters as functions of MEC position, thereby preserving the known anatomical organization of grid-cell properties.

Virtual animal trajectory

Grid-cell firing rates were driven by the trajectory of a virtual rat exploring a 60 × 60 cm square arena. Animal motion was generated by sampling velocities from uniform distributions specifying speed (0–30 cm/s), movement direction (0°–360°), and movement duration (0–500 ms). When a proposed trajectory exceeded the arena boundary, the velocity vector was reflected by 90°. Positions were updated at a sampling rate of 40 kHz and provided as input to the grid-map function, which generated time-varying firing rates.

Spike generation and refractoriness

Grid-cell firing rates were converted into spike trains using an inhomogeneous Poisson renewal process. At each simulation time step dt(ms), the instantaneous firing rate fr (Hz) was converted into a probability for spiking according to the following equation: $p = \frac{dt*fr}{1000}$, where dt is the time-step (ms), fr is the firing rate (Hz), and 1000 is a unit conversion factor to convert Hz to ms. Each time step was treated as a Bernoulli trial, and if a spike was generated, the subsequent probabilities were modified by multiplying them by an exponential function to represent the refractory period of the grid cell according to

$$\text{refractory}(t) = \begin{cases} 1 - e^{-(t-t_s)/\tau}, & t \geq t_s \\ 0, & t < t_s, \end{cases}$$

with a time constant $\tau = 35$ ms, estimated from intracellular recordings[85].

LEC input

In contrast to MEC-driven spatial input, LEC activity was modeled as behavior-independent contextual input. LEC neurons were driven by homogeneous Poisson renewal processes with fixed mean firing rates, reflecting experimental observations that LEC responses are weakly modulated by spatial position but strongly influenced by environmental content and novelty. This simplified representation isolates the distinct functional contributions of MEC and LEC to hippocampal processing while maintaining biologically plausible input statistics.

Together, this input framework provides behaviorally relevant driving signals that enable the hippocampal network to operate under realistic exploratory conditions while preserving the functional distinction between spatial and non-spatial entorhinal inputs.

Two-stage optimization framework

Model parameters were optimized to align neuronal and network dynamics with experimentally reported electrophysiological constraints. Optimization was performed hierarchically in two stages, progressing from single-neuron-level to neuronal-network-level dynamics, while preserving anatomically constrained connectivity[50] (**Fig. 4b**).

Single-neuron-level optimization of synaptic dynamics

Synaptic parameters were first optimized at the single-neuron level to reproduce experimentally measured unitary PSP waveforms. PSP dynamics were quantified using peak amplitude (AMP) and half-height width (HHW). For a given synapse from presynaptic neuron i to postsynaptic neuron j, PSP was simulated by activating the synapse with single-neuron-level synaptic parameters, conductance $w_{i,j}^{s}$ and time constant $\tau_{i,j}^{s}$, onto the postsynaptic Izhikevich neuron held at rest. The single-neuron-level loss function was defined as the sum of absolute errors between simulated and target PSP metrics: $L^{s} = |e(AMP)| + |e(HHW)|$. A quadratic optimization method was used to iteratively update synaptic parameters until convergence (**Fig. 4b**).

To reduce parameter dimensionality for synapses with both fast and slow receptor components, their relative conductances and decay kinetics were constrained prior to connection-specific optimization. For excitatory synapses, the NMDAR/AMPAR conductance-ratio was determined by matching simulated AMPAR and NMDAR peak-current ratios to experimental measurements obtained at (-70) and (+40) mV, respectively, thereby accounting for receptor-specific driving forces and the voltage-dependent Mg^{2+} block of NMDARs[86,87]. For inhibitory synapses, the $GABA_BR/GABA_AR$ gain ratio was fixed at 0.07 based on available experimental measurements[88,89].

The slow receptor decay constants were constrained by empirical relationships derived from literature-reported and model-fitted receptor kinetics[89–101]:

$$\tau_{\mathrm{NMDA}} = 2.26\,\tau_{\mathrm{AMPA}} + 12.6\ \mathrm{ms}$$
$$\tau_{\mathrm{GABA_B}} = 4.60\,\tau_{\mathrm{GABA_A}} + 115.8\ \mathrm{ms}$$

These relationships were used to couple fast (τ_{AMPA}, τ_{GABA_A}) and slow (τ_{NMDA}, τ_{GABA_B}) decay kinetics and reduce the number of independently optimized parameters.

For connections constrained by an isolated fast-component PSP, the slow-component gain was set to zero, and w and τ_{fast} were jointly optimized. For connections containing both fast and slow components, the slow-to-fast conductance ratio was fixed, while w and τ_{fast} were optimized; τ_{slow} was calculated from the corresponding empirical relationship at each candidate value of τ_{fast}.

After convergence, time constants $\tau_{i,j}^{s}$ were fixed. Synaptic conductances $w_{i,j}^{s}$ were used as initial values for the subsequent network-level optimization. For each presynaptic-to-postsynaptic projection, a single optimized parameter set was shared across the entire population. For simplicity, the subsequent network-level optimization denotes synaptic conductance and decay time constant by w and τ, respectively, since the fast and slow components are coupled, and therefore, each is represented by a single independent degree of freedom.

Network-level optimization of synaptic weights

Following single-neuron-level optimization of individual synapse types, network-level synaptic conductances $w_{i,j}^{s}$ were collectively optimized to reproduce *in vivo* population activity (**Fig. 4b**). The network objective incorporated three complementary measures: mean firing rate (R), population correlation (C), and oscillatory band power (O). We denote these measures by $M_k^{(q)}$, where k indexes the neuronal population and $q \in \{R, C, O\}$ denotes the activity measures. For each measure, the corresponding loss was defined as the difference between the simulated and target values as:

$$L_q = \sum_k \left| M_k^{(q),\mathrm{sim}} - M_k^{(q),\mathrm{target}} \right| / \left| M_k^{(q),\mathrm{target}} \right|$$

When multiple frequency bands were considered, the oscillatory measure was evaluated separately for each band and averaged. The overall network-level loss was $L^n = \sum_q L_q$.

Unlike single-neuron-level optimization, which involved only two parameters and single-neuron simulation, network-level optimization was high-dimensional and required full-network simulation. To efficiently navigate the high-dimensional, non-convex parameter space, we developed a hybrid optimization method that combines the Nelder–Mead simplex search with physiologically informed initialization and updates (**Fig. 4b**).

The optimization was initialized by evaluating the network using the results of the single-neuron-level optimization$w_{i,j}^{s}$ as initial values. $M_k^{(q)}$ were measured over a time window (2 seconds) to ensure stable measurements. The initial simplex was biased toward directions suggested by physiological insights; for example, firing rates below target prompted increases in excitatory or decreases in inhibitory conductances. However,

parameter exploration was allowed to cover the full range $(0.1\, w_{i,j}^{s}, 10\, w_{i,j}^{s})$ so all physiologically possible values could be explored. Standard Nelder–Mead operations, i.e., reflection, expansion, contraction, and shrinkage, were then applied to generate candidate solutions. An additional physiologically informed candidate w_{informed} was introduced and retained if it outperformed all simplex vertices. The worst-performing vertex was then replaced, and the procedure iterated as in the standard Nelder–Mead method (**Fig. 4b**).

This hybrid strategy integrates gradient-based physiological insights into a gradient-agnostic Nelder–Mead framework with minimal additional computational overhead. The Nelder–Mead component provides robustness when gradients are unreliable, while physiologically informed updates accelerate convergence when local physiological information is beneficial.

GPU-accelerated online parameter updating

Network-level optimization was performed during continuous simulation using CARLsim6's built-in *scaleWeights* functionality[48] that enables synaptic weights to be updated on the fly without resetting the network state or re-invoking large, initial transients (**Fig. 1c**). This approach reduces computational overhead, preserves temporal continuity, and enables efficient evaluation and optimization of network dynamics over behaviorally relevant timescales.

The *scaleWeights* function is thread-safe and supports hybrid computing environments with up to 24 CPUs and 8 GPUs on both bare-metal servers and virtualized clusters. CARLsim6 employs a dedicated host-side *manager* process that coordinates spiking neuronal network simulation at discrete 1-millisecond time steps. Before each simulation step, the synaptic weights of a specified connection group can be updated by its connection-group identifier. The corresponding weight block is first transferred from GPU device memory to host memory using a high-performance block-copy operation. The *manager* then scales all weights in the connection group by a specified scalar factor, after which the updated block is transferred back to device memory. This mechanism enables efficient online modification of synaptic parameters during ongoing simulation and is designed to operate with up to 789 GB of distributed GPU memory.

Simulation platform, hardware, and large-scale network support

All simulations were performed using CARLsim, a GPU-accelerated spiking neuronal network simulator designed for large-scale, biologically grounded network models[48]. CARLsim exploits the inherent parallelism of spiking neuronal networks by distributing neuron and synapse computations across massively parallel GPU kernels (**Fig. 1c**). Neuronal dynamics were updated at a fixed 0.1-ms simulation step, with event-driven synaptic processing to reduce computation under sparse-firing conditions. Memory-efficient data structures supported large, heterogeneous connectivity graphs, multiple receptor types, and axonal conduction delays.

As part of this project, CARLsim6 was extended and optimized to support anatomically constrained, large-scale hippocampal models[38,39]. A very-large-scale (VLS) configuration increased the maximum number of supported neuron groups from 96 to 211 and connection groups from 256 to 32,000, enabling representation of the large number of cell-type- and pathway-specific connections in the hippocampal model. Runtime memory structures were reorganized for efficient multi-GPU partitioning and multithreaded execution, and additional functionality enabled neuronal and synaptic parameters to be modified during ongoing simulations and custom optimization routines to be integrated directly into the simulation loop.

The multi-GPU implementation supports hybrid computing systems with up to 8 GPUs and 24 CPUs, enabling the distribution of network state and computational load across devices. For smaller networks, however, inter-device communication can offset the benefits of parallel execution; previous benchmarking of standard 80/20 cortical networks identified a crossover at approximately 300,000 neurons[102]. We therefore implemented the model used in this study at one-tenth scale, comprising approximately 250,000 neurons and 20 million synapses. This scale preserved the complete anatomical organization, neuronal diversity, and pathway structure while providing shorter turnaround times for iterative parameter optimization and validation.

Despite its reduced scale, the model remains computationally demanding due to its heterogeneous synaptic architecture and the use of the nine-parameter Izhikevich neuron model, which was numerically integrated using a fourth-order Runge–Kutta (RK4) method

with 10 integration steps per millisecond. At this network size, single-GPU execution avoided multi-device communication overhead and provided the most efficient configuration. Simulations and benchmarks reported here were therefore performed primarily on a single NVIDIA Quatro RTX 6000 GPU with 105 GB of CPU memory and 24 GB of GPU memory.

Scaling to the full-sized model

Scaling to the full-sized hippocampal model requires partitioning network state and computation across multiple GPUs while balancing computational and memory loads and minimizing inter-GPU communication. We designed an anatomically informed partitioning strategy in which the hippocampal network is divided along its longitudinal axis into slices spanning EC, DG, CA3, and CA1. Each partition, therefore, contains the major local circuitry and complete trisynaptic pathway from EC through DG and CA3 to CA1 (**Fig. 2b**).

This strategy leverages the intrinsic topographic organization of hippocampal connectivity as represented in the model. Because inter-region projections were constructed from tracer-derived spatial probability distributions, neurons preferentially connect to anatomically corresponding portions of downstream regions, with connectivity generally becoming sparser as longitudinal separation increases. Grouping corresponding portions of EC, DG, CA3, and CA1 within the same computational partition therefore maximized within-partition connectivity while reducing synaptic communication across GPUs and preserving functionally coherent circuit modules.

Computational scaling measurements further support the feasibility of full-scale simulation (**Fig. 4a**). Independent extrapolations based on neuron and synapse counts yielded closely agreeing estimates of approximately 700 GB of CPU RAM, 144 GB of GPU memory, and a runtime factor of ~50 for the full-sized network. Although these requirements exceed the resources of the single-GPU workstation used in the present study, the estimated GPU memory requirement is within the aggregate capacity of current high-memory multi-GPU systems. In addition, runtime exhibited sublinear scaling with network size over the benchmarked range, indicating that computational cost increased more slowly than network size.

Together, CARLsim6's distributed multi-GPU architecture, anatomically informed partitioning, and the measured scaling characteristics provide a computational pathway from the one-tenth-scale model used for efficient optimization and validation in this study to full-scale hippocampal simulation while preserving the model's anatomical, cellular, and synaptic organization.

Data availability

The synthetic data generated using the large-scale model of the hippocampus will be publicly available on GitHub at: https://github.com/neural-modeling-and-interface-lab/ upon publication.

Code availability

The code supporting this study will be available on GitHub at: https://github.com/neural-modeling-and-interface-lab/ upon publication.

Acknowledgement

This research was supported by NIH/NIDA BRAIN Initiative-Theories, Models and Methods (TMM) program (RF1DA055665/1R01EB031680).

Author contributions

G.Y. and C.X.: methodology, software, formal analysis, investigation, data curation, writing – original draft, review & editing, visualization. X.Z.: methodology, software, formal analysis, investigation. L.N.: methodology, software, formal analysis, investigation, data curation, writing – review & editing. H.D.: conceptualization, methodology, investigation. D.S.: conceptualization, methodology, formal analysis, investigation, writing – original draft, review & editing, visualization, supervision, project administration, funding acquisition.

Competing interest

The authors declare no competing interests.

References

1. O'Keefe, J. & Dostrovsky, J. The hippocampus as a spatial map. Preliminary evidence from unit activity in the freely-moving rat. *Brain Res.* **34**, (1971).

2. Hafting, T., Fyhn, M., Molden, S., Moser, M.-B. & Moser, E. I. Microstructure of a spatial map in the entorhinal cortex. *Nature* **436**, 801–6 (2005).

3. Taube, J. S., Muller, R. U. & Ranck, J. B. Head-direction cells recorded from the postsubiculum in freely moving rats. I. Description and quantitative analysis. *Journal of Neuroscience* https://doi.org/10.1523/jneurosci.10-02-00420.1990 (1990) doi:10.1523/jneurosci.10-02-00420.1990.

4. Solstad, T., Boccara, C. N., Kropff, E., Moser, M.-B. & Moser, E. I. Representation of Geometric Bordersin the Entorhinal Cortex. *Science* **1865**, 1–5 (2008).

5. Kropff, E., Carmichael, J. E., Moser, M. B. & Moser, E. I. Speed cells in the medial entorhinal cortex. *Nature 2015 523:7561* **523**, 419–424 (2015).

6. Dragoi, G. & Buzsáki, G. Temporal Encoding of Place Sequences by Hippocampal Cell Assemblies. *Neuron* **50**, 145–157 (2006).

7. MacDonald, C. J., Lepage, K. Q., Eden, U. T. & Eichenbaum, H. Hippocampal 'time cells' bridge the gap in memory for discontiguous events. *Neuron* **71**, (2011).

8. Kraus, B. J., Robinson, R. J., White, J. A., Eichenbaum, H. & Hasselmo, M. E. Hippocampal 'Time Cells': Time versus Path Integration. *Neuron* **78**, 1090–1101 (2013).

9. Stackman, R. W., Clark, A. S. & Taube, J. S. Hippocampal spatial representations require vestibular input. *Hippocampus* **12**, 291–303 (2002).

10. Deshmukh, S. S. & Knierim, J. J. Representation of non-spatial and spatial information in the lateral entorhinal cortex. *Front. Behav. Neurosci.* **5**, 14849 (2011).

11. Eichenbaum, H., Kuperstein, M., Fagan, A. & Nagode, J. Cue-sampling and goal-approach correlates of hippocampal unit activity in rats performing an odor-discrimination task. *Journal of Neuroscience* **7**, 716–732 (1987).

12. Herzog, L. E. *et al.* Interaction of Taste and Place Coding in the Hippocampus. *Journal of Neuroscience* **39**, 3057–3069 (2019).

13. Aronov, D., Nevers, R. & Tank, D. W. Mapping of a non-spatial dimension by the hippocampal–entorhinal circuit. *Nature 2017 543:7647* **543**, 719–722 (2017).

14. Scoville, W. B. & Milner, B. Loss of recent memory after bilateral hippocampal lesions. *J. Neurol. Neurosurg. Psychiatry* **20**, (1957).

15. Squire, L. R. Memory and the hippocampus - a synthesis from findings with rats, monkeys, and humans. *Psychol. Rev.* **99**, 195–231 (1992).

16. Bird, C. M. & Burgess, N. The hippocampus and memory: insights from spatial processing. *Nature Reviews Neuroscience 2008 9:3* **9**, 182–194 (2008).

17. Shapiro, M. L. & Eichenbaum, H. Hippocampus as a memory map: Synaptic plasticity and memory encoding by hippocampal neurons. *Hippocampus* **9**, 365–384 (1999).

18. Jarrard, L. E. Selective hippocampal lesions: Differential effects on performance by rats of a spatial task with preoperative versus postoperative training. *J. Comp. Physiol. Psychol.* **92**, 1119–1127 (1978).

19. Squire, L. R. & Alvarez, P. Retrograde amnesia and memory consolidation: a neurobiological perspective. *Curr. Opin. Neurobiol.* **5**, 169–177 (1995).

20. Nadel, L. & Moscovitch, M. Memory consolidation, retrograde amnesia and the hippocampal complex. *Curr. Opin. Neurobiol.* **7**, 217–227 (1997).

21. Winocur, G., Moscovitch, M. & Bontempi, B. Memory formation and long-term retention in humans and animals: Convergence towards a transformation account of hippocampal–neocortical interactions. *Neuropsychologia* **48**, 2339–2356 (2010).

22. Epstein, R. A., Patai, E. Z., Julian, J. B. & Spiers, H. J. The cognitive map in humans: spatial navigation and beyond. *Nature Neuroscience 2017 20:11* **20**, 1504–1513 (2017).

23. Eichenbaum, H. The role of the hippocampus in navigation is memory. *https://doi.org/10.1152/jn.00005.2017* **117**, 1785–1796 (2017).

24. Buzsáki, G. & Moser, E. I. Memory, navigation and theta rhythm in the hippocampal-entorhinal system. *Nature Neuroscience 2013 16:2* **16**, 130–138 (2013).

25. Markram, H. *et al.* Reconstruction and Simulation of Neocortical Microcircuitry. *Cell* **163**, 456–492 (2015).

26. Dura-Bernal, S. *et al.* Multiscale model of primary motor cortex circuits predicts in vivo cell-type-specific, behavioral state-dependent dynamics. *Cell Rep.* **42**, 112574 (2023).

27. Dura-Bernal, S. *et al.* Large-Scale Mechanistic Models of Brain Circuits with Biophysically and Morphologically Detailed Neurons. *Journal of Neuroscience* **44**, (2024).

28. Romani, A. *et al.* Community-based reconstruction and simulation of a full-scale model of the rat hippocampus CA1 region. *PLoS Biol.* **22**, e3002861 (2024).

29. Reimann, M. W. *et al.* Modeling and simulation of neocortical micro- and mesocircuitry (Part I, anatomy). *Elife* **13**, (2026).

30. Isbister, J. B. *et al.* Modeling and simulation of neocortical micro- and mesocircuitry (Part II, Physiology and experimentation). *Elife* **13**, (2026).

31. Hendrickson, P. J. P. J., Yu, G. J. G. J., Song, D. & Berger, T. W. T. W. A million-plus neuron model of the hippocampal dentate gyrus: Critical role for topography in determining spatiotemporal network dynamics. *IEEE Trans. Biomed. Eng.* **63**, 199–209 (2016).

32. Yu, G. J., Hendrickson, P. J., Song, D. & Berger, T. W. Spatiotemporal Patterns of Granule Cell Activity Revealed by a Large-Scale, Biologically Realistic Model of the Hippocampal Dentate Gyrus. in *Hippocampal Microcircuits* 473–508 (Springer, Cham, 2018). doi:10.1007/978-3-319-99103-0_12.

33. Potjans, T. C. & Diesmann, M. The Cell-Type Specific Cortical Microcircuit: Relating Structure and Activity in a Full-Scale Spiking Network Model. *Cerebral Cortex* **24**, 785–806 (2014).

34. Shi, J., Tripp, B., Shea-Brown, E., Mihalas, S. & Buice, M. A. MouseNet: A biologically constrained convolutional neural network model for the mouse visual cortex. *PLoS Comput. Biol.* **18**, e1010427 (2022).

35. Kopsick, J. D. *et al.* Robust Resting-State Dynamics in a Large-Scale Spiking Neural Network Model of Area CA3 in the Mouse Hippocampus. *Cognitive Computation 2021 15:4* **15**, 1190–1210 (2022).

36. Pronold, J. *et al.* Multi-scale spiking network model of human cerebral cortex. *Cerebral Cortex* **34**, (2024).

37. Yu, G. J., Bouteiller, J. M. C. & Berger, T. W. Topographic Organization of Correlation Along the Longitudinal and Transverse Axes in Rat Hippocampal CA3 Due to Excitatory Afferents. *Front. Comput. Neurosci.* **14**, 588881 (2020).

38. Yu, G. J., Xu, C., Niedermeier, L. & Song, D. Combined mechanistic and input-output modeling of the hippocampus: Towards a full-scale neuronal network model of rat hippocampus with anatomically-realistic connectivity. in *10th Annual BRAIN Initiative Meeting* (2024).

39. Yu, G. J., Xu, C., Bienkowski, M. & Song, D. Combined mechanistic and input-output modeling of the hippocampus: GPU-accelerated large-scale model of rat hippocampus with topographically organized connectivity. in *9th Annual BRAIN Initiative Meeting* (2023).

40. Yu, G. J. & Song, D. Combined mechanistic and input-output modeling of the hippocampus: Full-scale biologically realistic model of hippocampus. in *8th Annual BRAIN Initiative Meeting* (Washington, D.C., 2022).

41. Fanselow, M. S. & Dong, H. W. Are the Dorsal and Ventral Hippocampus Functionally Distinct Structures? *Neuron* **65**, 7–19 (2010).

42. Dong, H. W., Swanson, L. W., Chen, L., Fanselow, M. S. & Toga, A. W. Genomic-anatomic evidence for distinct functional domains in hippocampal field CA1. *Proc. Natl. Acad. Sci. U. S. A.* **106**, 11794–11799 (2009).

43. Bienkowski, M. S. *et al.* Integration of gene expression and brain-wide connectivity reveals the multiscale organization of mouse hippocampal networks. *Nat. Neurosci.*

https://doi.org/10.1038/s41593-018-0241-y (2018) doi:10.1038/s41593-018-0241-y.

44. Wheeler, D. W. *et al.* Hippocampome.org: a knowledge base of neuron types in the rodent hippocampus. *Elife* **4**, e09960 (2015).

45. Wheeler, D. W. *et al.* Hippocampome.org 2.0 is a knowledge base enabling data-driven spiking neural network simulations of rodent hippocampal circuits. *Elife* **12**, (2024).

46. Buckmaster, P. S., Wenzel, H. J., Kunkel, D. D. & Schwartzkroin, P. A. Axon arbors and synaptic connections of hippocampal mossy cells in the rat in vivo. *Journal of Comparative Neurology* **366**, 270–292 (1996).

47. Hendrickson, P. J., Yu, G. J., Song, D. & Berger, T. W. Interactions between Inhibitory Interneurons and Excitatory Associational Circuitry in Determining Spatio-Temporal Dynamics of Hippocampal Dentate Granule Cells: A Large-Scale Computational Study. *Front. Syst. Neurosci.* **9**, (2015).

48. Niedermeier, L. *et al.* CARLsim 6: An Open Source Library for Large-Scale, Biologically Detailed Spiking Neural Network Simulation. *Proceedings of the International Joint Conference on Neural Networks* https://doi.org/10.1109/IJCNN55064.2022.9892644 (2022) doi:10.1109/IJCNN55064.2022.9892644.

49. Izhikevich, E. M. *Dynamical Systems in Neuroscience*. (MIT press, 2007).

50. Xu, C., Yu, G. J., Niedermeier, L., Zhang, X. & Song, D. Biologically constrained Nelder-Mead optimization of a large-scale mechanistic model of rat hippocampal CA1 area. in *Society for Neuroscience Abstracts* PSTR478.02 (2025).

51. Nelder, J. A. & Mead, R. A Simplex Method for Function Minimization. *Comput. J.* **7**, 308–313 (1965).

52. Yu, G. J., Bouteiller, J.-M. C., Song, D. & Berger, T. W. Axonal Anatomy Optimizes Spatial Encoding in the Rat Entorhinal-Dentate System: A Computational Study. *IEEE Trans. Biomed. Eng.* https://doi.org/10.1109/tbme.2019.2894410 (2019) doi:10.1109/tbme.2019.2894410.

53. Park, E. H., Dvorak, D. & Fenton, A. A. Ensemble Place Codes in Hippocampus: CA1, CA3, and Dentate Gyrus Place Cells Have Multiple Place Fields in Large Environments. *PLoS One* **6**, e22349 (2011).

54. Gandolfi, D. *et al.* Full-scale scaffold model of the human hippocampus CA1 area. *Nature Computational Science 2023 3:3* **3**, 264–276 (2023).

55. Romani, A. *et al.* Community-based reconstruction and simulation of a full-scale model of the rat hippocampus CA1 region. *PLoS Biol.* **22**, e3002861 (2024).

56. Tiddia, G. *et al.* Fast Simulation of a Multi-Area Spiking Network Model of Macaque Cortex on an MPI-GPU Cluster. *Front. Neuroinform.* **16**, 883333 (2022).

57. Alevi, D., Stimberg, M., Sprekeler, H., Obermayer, K. & Augustin, M. Brian2CUDA: Flexible and Efficient Simulation of Spiking Neural Network Models on GPUs. *Front. Neuroinform.* **16**, 883700 (2022).

58. Callaway, E. M. *et al.* A multimodal cell census and atlas of the mammalian primary motor cortex. *Nature 2021 598:7879* **598**, 86–102 (2021).

59. Ascoli, G. A. & Wheeler, D. W. In search of a periodic table of the neurons: Axonal-dendritic circuitry as the organizing principle: Patterns of axons and dendrites within distinct anatomical parcels provide the blueprint for circuit-based neuronal classification. *Bioessays* **38**, 969 (2016).

60. Song, D. Decoding Naturalistic Episodic Memory with Artificial Intelligence and Brain-Machine Interface. *Advanced Science* **13**, e20125 (2026).

61. She, X. *et al.* Distributed Temporal Coding of Visual Memory Categories in Human Hippocampal Neurons Revealed by an Interpretable Decoding Model. *Advanced Science* https://doi.org/10.1002/advs.202502047 (2025) doi:10.1002/advs.202502047.

62. Song, D. *et al.* Sparse Large-Scale Nonlinear Dynamical Modeling of Human Hippocampus for Memory Prostheses. *IEEE Transactions on Neural Systems and Rehabilitation Engineering* **26**, 272–280 (2018).

63. Song, D. *et al.* Parametric and non-parametric modeling of short-term synaptic plasticity. Part I: Computational study. *J. Comput. Neurosci.* **26**, 21–37 (2009).

64. Song, D., Wang, Z., Marmarelis, V. Z. & Berger, T. W. Parametric and non-parametric modeling of short-term synaptic plasticity. Part II: Experimental study. *J. Comput. Neurosci.* https://doi.org/10.1007/s10827-008-0098-2 (2009) doi:10.1007/s10827-008-0098-2.

65. Pagkalos, M., Chavlis, S. & Poirazi, P. Introducing the Dendrify framework for incorporating dendrites to spiking neural networks. *Nature Communications 2023 14:1* **14**, 131- (2023).

66. Swanson, L. W., Wyss, J. M. & Cowan, W. M. An autoradiographic study of the organization of intrahippocampal association pathways in the rat. *J Comp Neurol* **181**, 681–715 (1978).

67. Swanson, L. W. & Cowan, W. M. An autoradiographic study of the organization of the efferet connections of the hippocampal formation in the rat. *Journal of Comparative Neurology* **172**, 49–84 (1977).

68. Ropireddy, D., Bachus, S. E. & Ascoli, G. A. Non-homogeneous stereological properties of the rat hippocampus from high-resolution 3D serial reconstruction of thin histological sections. *Neuroscience* **205**, 91–111 (2012).

69. Dolorfo, C. L. & Amaral, D. G. Entorhinal cortex of the rat: Topographic organization of the cells of origin of the perforant path projection to the dentate gyrus. *Journal of Comparative Neurology* **398**, 25–48 (1998).

70. Gaarskjaer, F. B. Organization of the mossy fiber system of the rat studied in extended hippocampi. I. Terminal area related to number of granule and pyramidal cells. *Journal of Comparative Neurology* **178**, 49–71 (1978).

71. Ishizuka, N., Weber, J. & Amaral, D. G. Organization of intrahippocampal projections originating from CA3 pyramidal cells in the rat. *Journal of Comparative Neurology* **295**, 580–623 (1990).

72. West, M. J., Slomianka, L. & Gundersen, H. J. G. Unbiased stereological estimation of the total number of neurons in the subdivisions of the rat hippocampus using the optical fractionator. *Anat. Rec.* **231**, 482–497 (1991).

73. Patton, P. E. & McNaughton, B. Connection matrix of the hippocampal formation: I. The dentate gyrus. *Hippocampus* **5**, 245–286 (1995).

74. Gulyás, A. I., Megías, M., Emri, Z. & Freund, T. F. Total Number and Ratio of Excitatory and Inhibitory Synapses Converging onto Single Interneurons of Different Types in the CA1 Area of the Rat Hippocampus. *Journal of Neuroscience* **19**, 10082–10097 (1999).

75. Megías, M., Emri, Z., Freund, T. F. & Gulyás, A. I. Total number and distribution of inhibitory and excitatory synapses on hippocampal CA1 pyramidal cells. *Neuroscience* **102**, 527–540 (2001).

76. Crain, B., Cotman, C., Taylor, D. & Lynch, G. A quantitative electron microscopic study of synaptogenesis in the dentate gyrus of the rat. *Brain Res.* **63**, 195–204 (1973).

77. Acsády, L., Kamondi, A., Sík, A., Freund, T. & Buzsáki, G. GABAergic Cells Are the Major Postsynaptic Targets of Mossy Fibers in the Rat Hippocampus. *Journal of Neuroscience* **18**, 3386–3403 (1998).

78. Tamamaki, N. & Nojyo, Y. Projection of the entorhinal layer II neurons in the rat as revealed by intracellular pressure-injection of neurobiotin. *Hippocampus* **3**, 471–480 (1993).

79. Li, X. -G, Somogyi, P., Ylinen, A. & Buzsáki, G. The hippocampal CA3 network: An in vivo intracellular labeling study. *Journal of Comparative Neurology* **339**, 181–208 (1994).

80. Roth, A. & van Rossum, M. C. W. Modeling Synapses. *Computational Modeling Methods for Neuroscientists* 139–160 (2009) doi:10.7551/MITPRESS/9780262013277.003.0007.

81. Mayer, M. L., Westbrook, G. L. & Guthrie, P. B. Voltage-dependent block by Mg2+ of NMDA responses in spinal cord neurones. *Nature 1984 309:5965* **309**, 261–263 (1984).

82. Jahr, C. E. & Stevens, C. F. A quantitative description of NMDA receptor-channel kinetic behavior. *Journal of Neuroscience* **10**, 1830–1837 (1990).

83. Blair, H. T., Welday, A. C. & Zhang, K. Scale-Invariant Memory Representations Emerge from Moiré Interference between Grid Fields That Produce Theta Oscillations: A Computational Model. *Journal of Neuroscience* **27**, 3211–3229 (2007).

84. Stensola, H. *et al.* The entorhinal grid map is discretized. *Nature 2012 492:7427* **492**, 72–78 (2012).

85. Alonso, A. & Klink, R. Differential electroresponsiveness of stellate and pyramidal-like cells of medial entorhinal cortex layer II. *https://doi.org/10.1152/jn.1993.70.1.128* **70**, 128–143 (1993).

86. Booker, S. A., Sumera, A., Kind, P. C. & Wyllie, D. J. A. Contribution of NMDA Receptors to Synaptic Function in Rat Hippocampal Interneurons. *eNeuro* **8**, (2021).

87. Wang, Z., Song, D. & Berger, T. W. Contribution of NMDA receptor channels to the expression of LTP in the hippocampal dentate gyrus. *Hippocampus* **12**, 680–688 (2002).

88. Scanziani, M. GABA spillover activates postsynaptic GABA(B) receptors to control rhythmic hippocampal activity. *Neuron* **25**, 673–681 (2000).

89. Price, C. J., Scott, R., Rusakov, D. A. & Capogna, M. GABAB Receptor Modulation of Feedforward Inhibition through Hippocampal Neurogliaform Cells. *Journal of Neuroscience* **28**, 6974–6982 (2008).

90. Li, S. *et al.* Determination of effective synaptic conductances using somatic voltage clamp. *PLoS Comput. Biol.* **15**, e1006871 (2019).

91. Hestrin, S., Sah, P. & Nicoll, R. A. Mechanisms generating the time course of dual component excitatory synaptic currents recorded in hippocampal slices. *Neuron* **5**, 247–253 (1990).

92. Sah, P., Hestrin, S. & Nicoll, R. A. Properties of excitatory postsynaptic currents recorded in vitro from rat hippocampal interneurones. *J. Physiol.* **430**, 605–616 (1990).

93. Otmakhova, N. A., Otmakhov, N. & Lisman, J. E. Pathway-Specific Properties of AMPA and NMDA-Mediated Transmission in CA1 Hippocampal Pyramidal Cells. *The Journal of Neuroscience* **22**, 1199 (2002).

94. Roepstorff, A. & Lambert, J. D. C. Factors contributing to the decay of the stimulus-evoked IPSC in rat hippocampal CA1 neurons. *J. Neurophysiol.* **72**, 2911–2926 (1994).

95. Hefft, S. & Jonas, P. Asynchronous GABA release generates long-lasting inhibition at a hippocampal interneuron-principal neuron synapse. *Nat. Neurosci.* **8**, 1319–1328 (2005).

96. Otis, T. S., De Koninck, Y. & Mody, I. Characterization of synaptically elicited GABAB responses using patch-clamp recordings in rat hippocampal slices. *J. Physiol.* **463**, 391–407 (1993).

97. Liu, Y. C., Cheng, J. K. & Lien, C. C. Rapid Dynamic Changes of Dendritic Inhibition in the Dentate Gyrus by Presynaptic Activity Patterns. *Journal of Neuroscience* **34**, 1344–1357 (2014).

98. Mott, D. D., Li, Q., Okazaki, M. M., Turner, D. A. & Lewis, D. V. GABAB-Receptor–Mediated Currents in Interneurons of the Dentate-Hilus Border. *https://doi.org/10.1152/jn.1999.82.3.1438* **82**, 1438–1450 (1999).

99. Savanthrapadian, S. *et al.* Synaptic Properties of SOM- and CCK-Expressing Cells in Dentate Gyrus Interneuron Networks. *The Journal of Neuroscience* **34**, 8197 (2014).

100. Armstrong, C., Szabadics, J., Tamás, G. & Soltesz, I. Neurogliaform Cells in the Molecular Layer of the Dentate Gyrus as Feed-Forward γ-Aminobutyric Acidergic

Modulators of Entorhinal–Hippocampal Interplay. *J. Comp. Neurol.* **519**, 1476 (2011).

101. Booker, S. A. *et al.* Differential GABAB-receptor-mediated effects in perisomatic- and dendrite-targeting parvalbumin interneurons. *J. Neurosci.* **33**, 7961–7974 (2013).

102. Chou, T. S. *et al.* CARLsim 4: An Open Source Library for Large Scale, Biologically Detailed Spiking Neural Network Simulation using Heterogeneous Clusters. *Proceedings of the International Joint Conference on Neural Networks* **2018-July**, (2018).

Supplementary Files

This is a list of supplementary files associated with this preprint. Click to download.

- HippoModelmssupplv1.docx